Chapter 10

Remote Sensing

J. BÜHL,[a] S. ALEXANDER,[b,c] S. CREWELL,[d] A. HEYMSFIELD,[e] H. KALESSE,[a] A. KHAIN,[f] M. MAAHN,[g,h] K. VAN TRICHT,[i] AND M. WENDISCH[j]

[a] *Leibniz Institute for Tropospheric Research, Leipzig, Germany*
[b] *Australian Antarctic Division, Kingston, Tasmania, Australia*
[c] *Antarctic Climate and Ecosystems Co-operative Research Centre, University of Tasmania, Hobart, Tasmania, Australia*
[d] *University of Cologne, Cologne, Germany*
[e] *Physical Meteorology Section, Mesoscale and Microscale Meteorology Laboratory, NCAR, Boulder, Colorado*
[f] *Hebrew University of Jerusalem, Jerusalem, Israel*
[g] *University of Colorado Boulder, Boulder, Colorado*
[h] *NOAA/Earth System Research Laboratory, Boulder, Colorado*
[i] *University of Leuven, Leuven, Belgium*
[j] *Leipzig Institute for Meteorology, Leipzig, Germany*

ABSTRACT

State-of-the-art remote sensing techniques applicable to the investigation of ice formation and evolution are described. Ground-based and spaceborne measurements with lidar, radar, and radiometric techniques are discussed together with a global view on past and ongoing remote sensing measurement campaigns concerned with the study of ice formation and evolution. This chapter has the intention of a literature study and should illustrate the major efforts that are currently taken in the field of remote sensing of atmospheric ice. Since other chapters of this monograph mainly focus on aircraft in situ measurements, special emphasis is put on active remote sensing instruments and synergies between aircraft in situ measurements and passive remote sensing methods. The chapter concentrates on homogeneous and heterogeneous ice formation in the troposphere because this is a major topic of this monograph. Furthermore, methods that deliver direct, process-level information about ice formation are elaborated with a special emphasis on active remote sensing methods. Passive remote sensing methods are also dealt with but only in the context of synergy with aircraft in situ measurements.

1. Introduction

A major goal of remote sensing of ice in clouds is the measurement of cloud optical properties because ice-forming clouds can influence Earth's radiative properties (Fig. 10-1). Figure 10-1a indicates that the magnitude of the solar radiative cooling of mixed-phase clouds strongly depends on the ice content. The more ice is in the cloud, the less the solar cooling effect. This is mostly a result of the decreasing optical thickness of the cloud when the ice content increases. In this case, the ice crystals become larger, at the expense of the smaller liquid water droplets. Figure 10-1b shows that the sign of net (solar plus terrestrial) radiative effect of clouds can change from warming to cooling or vice versa depending on the ice water content in the cloud. For low sun elevations [large solar zenith angle (SZA)] such as in the Arctic, the overall effect of mixed-phase clouds seems to be warming. Clouds remain a highly uncertain component of the global climate system, and understanding of the relation between cloud microphysics, aerosols, life cycle, and optical properties is needed in order make projections about the future development of Earth's climate (Fan et al. 2016). This chapter summarizes how combined observations with optical instrumentation (active: lidars; passive: imaging spectrometers) and microwave sensors (active: radars; passive: microwave radiometers) can be used to derive crucial measurements about the microphysical, dynamical, and radiative properties of aerosols, clouds, and water vapor.

Recently, the polar regions of Earth came into focus. Arctic low-level mixed-phase clouds are found to pose significant challenges as they are often long-lived (Morrison et al. 2012) and are suspected to significantly

Corresponding author: J. Bühl, buehl@tropos.de

DOI: 10.1175/AMSMONOGRAPHS-D-16-0015.1

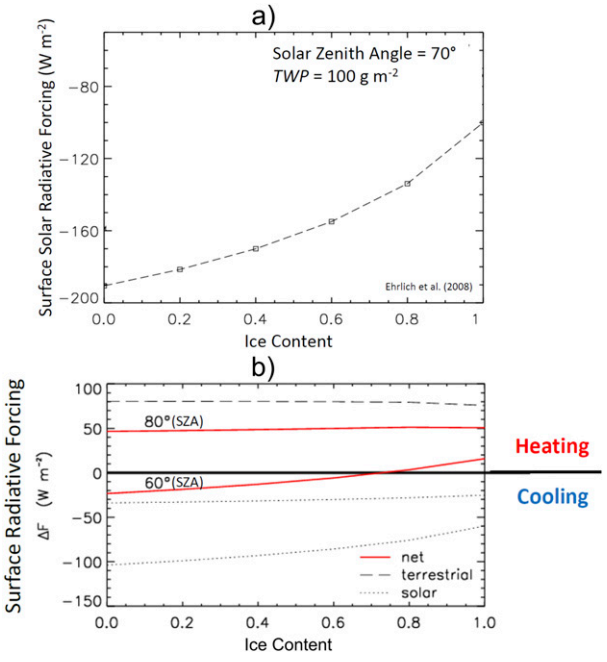

FIG. 10-1. Surface radiative forcing (W m^{-2}) as a function of ice content within clouds. (a) The solar radiative forcing, for an SZA of 70° and a total water path (TWP) of 100 g m^{-2}. (b) The solar (dotted), terrestrial (dashed), and net = solar plus terrestrial (red solid) surface radiative forcing are depicted. The figures are from Ehrlich et al. (2008) and Wendisch et al. (2013a).

contribute to the so-called Arctic amplification (Wendisch et al. 2013a, 2017)—an enhanced (factors of 2–3) increase of the near-surface air temperature compared to the generally observed global warming. The actual contribution of clouds to Arctic amplification still needs to be quantified (Cohen et al. 2014). For example, it depends—among many other factors—crucially on the ice content in the mixed-phase clouds. Also, in the Southern Ocean, clouds have turned out to be poorly understood and, thus, poorly represented in reanalyses and coupled climate models (Trenberth and Fasullo 2010; Naud et al. 2014). Model simulations and reanalyses suggest that a major contributor to this bias is a lack of clouds in the cold sectors of cyclones (Bodas-Salcedo et al. 2014). These Southern Ocean clouds contain a much lower proportion of ice at a given temperature than clouds in the Northern Hemisphere (Marchand et al. 2010), and ice formation in mixed-phase cloud layers has been found to be less efficient (Kanitz et al. 2011). Both phenomena could be attributed to the much cleaner atmosphere of the Southern Ocean with a smaller reservoir of ice nucleating particles.

Future land-, ship-, and aircraft-based experiments planned for the upcoming years in the northern and Southern Ocean will seek to address these issues. So far, satellite data have to be relied upon heavily in these regions because of the lack of ground-based observations.

Satellite data provide near-global coverage of cloud properties and are a crucial component for the evaluation and improvement of weather forecasting and climate models. The *CloudSat* (Stephens et al. 2002) and *Cloud–Aerosol Lidar and Infrared Pathfinder Satellite Observations* (*CALIPSO*; Winker et al. 2010) satellites allow, for the first time, to study ice cloud properties on a global scale with active remote sensing methods (Zhang et al. 2010). Both satellites were put into the same orbit, one following the other with a distance of about a hundred kilometers or 17 s. They were embedded into NASA's afternoon constellation (A-Train) of satellites. The new satellite Earth Clouds, Aerosols and Radiation Explorer (EarthCARE; Illingworth et al. 2015) of the European Space Agency (ESA) and Japan Aerospace Exploration Agency (JAXA) to be launched in 2018 will eventually combine the capabilities of spaceborne lidar and radar into one satellite. Combining sophisticated methods of ice detection in clouds with lidar and radar will be the starting point of a development that will enable us to follow the life cycle of a heterogeneously formed ice particle from the ice nucleus (Mamouri and Ansmann 2015), to ice nucleation, and toward the generation of rain. This development has already started, for example, with advanced *CALIPSO*/*CloudSat* products like radar–lidar cloud parameter retrieval (DARDAR; Delanoë and Hogan 2010; Battaglia and Delanoë 2013) and the EarthCARE mission.

It is an intention of this chapter to show that ground-based, airborne, and satelliteborne remote sensing instruments can deliver critical information about height levels of ice formation and the history of cloud ice and can, hence, be used to challenge the problems mentioned above. The length scales that can be observed by satellites are usually larger than for ground-based instrumentation, limiting the capability to directly observe cloud processes. Most ground-based remote sensing instruments can also be operated with limited effort on a continuous basis. During the recent two decades, combined remote sensing studies have been used for decades for long-term monitoring programs. Large efforts have been put into the development of frameworks such as the Atmospheric Radiation Measurement (ARM) program (Shupe et al. 2008; Miller et al. 2016) or Cloudnet (Illingworth et al. 2007) that process combined remote sensing data automatically and provide quality-assured data to users on an operational basis. For ground-based cloud radar systems, the development of innovative methods to detect ice-formation processes has occurred (Kollias et al. 2014; Myagkov et al. 2015, 2016), including the use of the wavelength dependence of radar attenuation. Such approaches will deliver new insights into the microphysical composition of clouds, including detailed information on particle size and shape (Smith et al. 2007; Kneifel et al. 2011). Recently, methods were developed to measure the amount of ice nucleating particles with ground-based Raman–depolarization lidar (Mamouri and

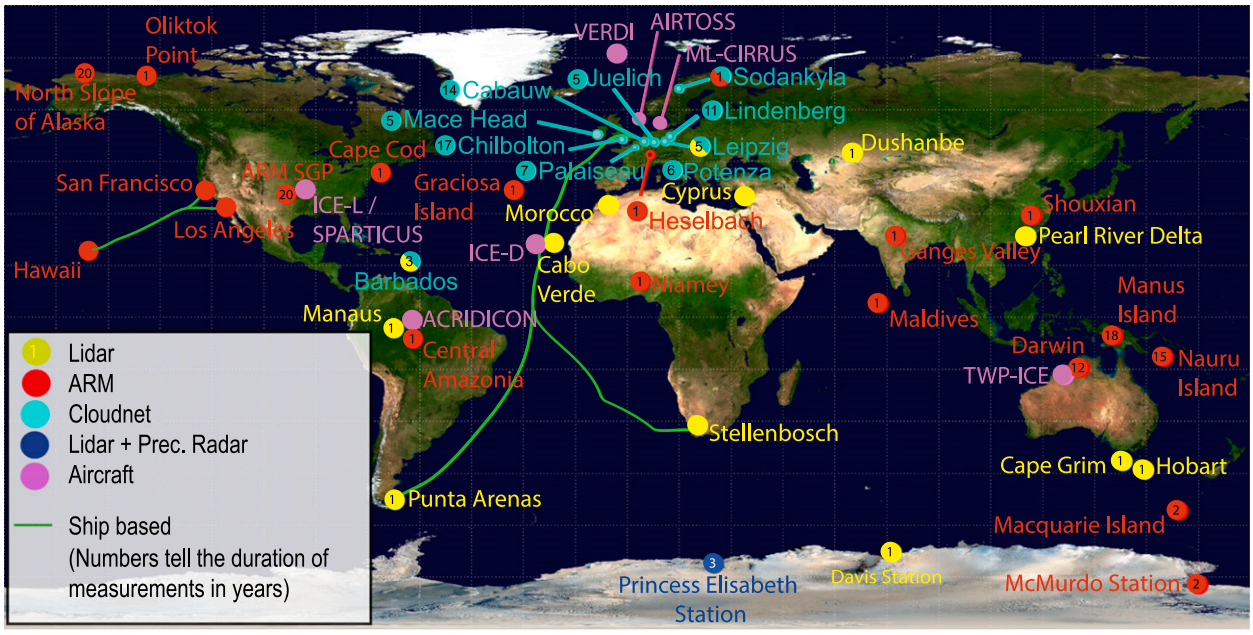

FIG. 10-2. Global remote sensing activities from ARM and Cloudnet programs, complemented by singular ground-based and ship-based lidar campaigns. The numbers in the circles tell the approximate duration of the respective measurements on site in years as of 2016. (Background: NASA.)

Ansmann 2015). In this way, information is provided about the ice-nucleating properties of aerosol particles at the level of ice nucleation, which adds quantitative information about the heterogeneous ice nucleation process. This process of ice formation in the troposphere always involves an ice nucleating particle, so that supercooled water can freeze below −36°C (Pruppacher and Klett 1997; Lohmann et al. 2016). Remote sensing of heterogeneous ice formation in mixed-phase clouds is challenging with any kind of instrumentation or sensor technique because the turbulent environment of the clouds in which ice particles are formed complicates the identification of the ice-formation process and distorts spectrally resolved measurements from cloud radars or Doppler lidars. In deep convective clouds, signal attenuation significantly limits the use of lidar and even radar instruments. Therefore, shallow mixed-phase cloud layers have recently been the main target for ice-formation studies (Fleishauer et al. 2002; Kanitz et al. 2011). In such clouds, ice formation is limited to the immersion freezing process (Ansmann et al. 2009b), and particles are mostly pristine when sedimenting from the mixed-phase cloud layer (Bühl et al. 2016).

Vertically resolved measurements have some advantages over in situ probing with aircraft, because the latter often deliver information from one height at a time (except for vertical ascents and descents) and may miss the level of actual ice formation. Lidar, radar, and passive sensors also measure remotely using electromagnetic emission, so they do not alter the probed cloud volume; they are less invasive than aircraft systems and can hence be used well in synergetic combination with in situ aircraft measurements. For that reason, airborne remote sensing measurements are the ideal partners in combined synergistic experiments together with in situ probing. Consequently, there have been several approaches combining lidar, radar, and in situ probing from aircraft (Wang et al. 2012; Maahn et al. 2015). Recent combinations of passive remote sensing sensors on towed platforms even challenge the common separation into in situ and remote sensing instruments (Werner et al. 2014; Finger et al. 2016). Also, spaceborne applications are suitably up valued by the synergy between passive optical imaging and active remote sensing (Anderson et al. 2005; Illingworth et al. 2015).

The following section yields a comprehensive overview about ground-based lidar and radar systems, combined lidar–radar satellites, microwave radiometry from ground and space, and combined aircraft in situ–remote sensing approaches to study ice formation and its evolution in the atmosphere.

2. Overview of remote sensing methods to study ice formation

a. Activities on a global scale and goals of ice remote sensing

During the last decade, numerous remote sensing campaigns were performed in order to study ice formation and evolution. In this section, an overview is given about the observation methods and their global application. Figure 10-2 gives an overview about many

TABLE 10-1. Overview about measurement campaigns related to ice formation also mentioned in Fig. 10-2.

Campaign location	Type	Duration (yr)	Data availability/website (if available)
Long-term measurement stations			
North Slope of Alaska, United States	ARM supersite	20[a]	Overview and data: www.arm.gov
Southern Great Plains, United States	ARM supersite	20[a]	Mather and Voyles (2013)
Manus Island, Papua New Guinea	ARM supersite	18	
Graciosa Island, Azores	ARM supersite	3[a]	
Darwin, Australia	ARM supersite	12	
Nauru Island	ARM supersite	15	
Cabauw, Netherlands	Cloudnet station	14[a]	Overview: www.cloud-net.org
Chilbolton, United Kingdom	Cloudnet station	17[a]	Public database: actris.nilu.no
Jülich, Germany	Cloudnet station	5[a]	Illingworth et al. (2007)
Leipzig, Germany	Cloudnet station	5[a]	
Lindenberg, Germany	Cloudnet station	11[a]	
Potenza, Italy	Cloudnet station	6[a]	
Palaiseau, France	Cloudnet station	7[a]	
Barbados	Cloudnet station	3[a]	
Sodankyla, Finland	Cloudnet station	1[a]	
Mace Head, Ireland	Cloudnet station	5[a]	
Princess Elisabeth, Antarctica	Lidar and precipitation radar	Since 2010	Gorodetskaya et al. (2015)
Short-duration measurement campaigns			
San Francisco/Los Angeles/Hawaii, United States	Ship-based ARM measurements	<1	Overview and data: www.arm.gov
Cape Cod, United States	ARM deployment	1	Miller et al. (2016)
Graciosa Island, Azores	ARM deployment	1	
Oliktok Point, United States	ARM deployment	1	
Central Amazonia, Brazil	ARM deployment	1	
Heselbach, Germany	Convective and Orographically-Induced Precipitation Study (COPS) measurements/ARM deployment	<1	
Ganges Valley, India	ARM deployment	1	
Niamey, Niger	ARM deployment	1	
Maldives	ARM deployment	1	
Shouxian, China	ARM deployment	1	
Macquarie Island, Australia	ARM deployment	2	
McMurdo Station, Antarctica	ARM deployment	2	
Morocco	Saharan Mineral Dust Experiment (SAMUM)-1 campaign	<1	Heintzenberg (2009)
Cape Verde	SAMUM-2 campaign	<1	Heintzenberg (2009)
Manaus, Brazil	Lidar campaign	1	Seifert et al. (2015)
Punta Arenas, Chile	Lidar campaign	1	Kanitz et al. (2011)
Stellenbosch, South Africa	Lidar campaign	1	Kanitz et al. (2011)
Pearl River Delta, China	Lidar campaign	<1	Ansmann et al. (2005)
Hobart, Australia	Lidar campaign	1	Huang et al. (2015)
Cape Grim, Australia	Lidar campaign	1	Alexander and Protat (2017, manuscript submitted to *J. Geophys. Res.*)
Davis Station, Antarctica	Lidar campaign	1	—
Dushanbe, Tajikistan	Central Asian Dust Experiment (CADEX) campaign (lidar)	2	—
Cyprus	Cyprus Aerosol, Clouds and Precipitation Experiment (CyCARE) campaign (lidar)	<1	—
Western Pacific (Darwin)	Tropical Warm Pool–International Cloud Experiment (TWP-ICE) (aircraft)	<1	May et al. (2008)
Rocky Mountains, Colorado	Ice in Clouds Experiment—Layer Clouds (ICE-L) (aircraft)	<1	Heymsfield et al. (2011)

TABLE 10-1. (*Continued*)

Campaign location	Type	Duration (yr)	Data availability/website (if available)
Cheltenham [Facility for Airborne Atmospheric Measurements (FAAM)]	Small Particles in Cirrus (SPARTICUS) (aircraft)	<1	Zhang et al. (2013)
Cape Verde	Ice in Clouds Experiment—Dust (ICE-D) (aircraft)	<1	—
Svalbard	Vertical Distribution of Ice in Arctic Mixed-Phase Clouds (VERDI) (aircraft)	<1	Klingebiel et al. (2015)
North Sea	AIRTOSS campaign	<1	Finger et al. (2016)
Central Europe	Midlatitude Cirrus Experiment (ML-CIRRUS)	<1	Voigt et al. (2017)
Central Amazonia	ACRIDICON	<1	Wendisch et al. (2016)

[a] Active measurement stations.

of the remote sensing campaigns that were performed within the last 20 years or are ongoing. The figure shows that ice-formation research is conducted globally and with significant efforts. An overview about the measurement campaigns in Fig. 10-2 is given in Table 10-1.

Figure 10-3 gives an overview about the objects and physical parameters that can be measured via remote sensing. From the climatological point of view, the most important parameters might be the ice water content (IWC), its corresponding ice water path (IWP), and the ice-effective radius (r_{eff}) because they have a large influence on the radiative transfer properties of an atmospheric volume. From the point of view of the actual ice-formation process, additionally, height level of ice formation, the corresponding temperature, and fall velocity might be most interesting because they tell where ice is formed and how it is evolving while falling through lower layers. From Fig. 10-3 it can already be seen that the study of ice formation and evolution cannot be performed with a single instrument but only a combination of several instruments and techniques can yield a clear picture.

b. Study of ice formation and evolution using ground-based lidar and radar

Ground-based lidars have been used for studying ice-formation processes (Ansmann et al. 2009a; Kanitz et al. 2011; see also Fig. 10-2). While a lidar alone provides information about the presence of ice particles (Seifert et al. 2010), a combination of lidar and cloud radars can be used to quantify the amount of ice and water present in clouds (Hogan et al. 2006; Westbrook and Illingworth 2013; Bühl et al. 2016).

From the physical point of view, lidars and radars are similar instruments. Both transmit and receive electromagnetic radiation, however, at different wavelengths. Lidars commonly operate in the optical (micrometer) wavelength range, while cloud radars emit radiation in the microwave (millimeter) wavelength range. The radiation that is scattered back from ice particles is consequently proportional to D^2 for lidars (geometrical scattering) and—for particles much smaller than the radar wavelength—D^6 for radars (Rayleigh scattering), with D indicating the volume-equivalent diameter of the particles. For particles larger than roughly 1/10th of the radar wavelength, the increase of backscattering with diameter is less than D^6, and other methods such as T matrix (Mishchenko 2000), Self-Similar Rayleigh–Gans (Hogan and Westbrook 2014), or the discrete dipole approximation (Draine and Flatau 1994) have to be used to estimate the backscattering of ice particles. Yet, the signals of both systems are strongly dominated by the largest particles in the observation volume. For radars, this effect is more dominant than for lidars. Therefore, a cloud radar is much better suited for the detection of large ice particles that appear in low numbers. However, a cloud radar can only partly detect the predominantly liquid parts of the clouds where droplets are small but numerous. Here, the lidar backscatter signal is strongest but also strongly attenuated. As a consequence, a lidar can often not see though liquid cloud layers. The particle-detection capability of modern cloud radars is impressive, as a cloud radar with a sensitivity of $-50\,\text{dB}Z$ at cloud level can detect one columnar ice particle with a length of about $200\,\mu\text{m}$ per cubic meter. Hence, the sensitivity is several magnitudes higher than, for example, that of typical precipitation radars, which have a typical lower signal threshold of about 0 dB. The higher sensitivity can be explained mainly by the closer range of observation (<12 km) and the shorter (millimeter range) wavelength. Airborne particle imagers would need long integration times in order to detect a significant amount of ice particles under such conditions. This illustrates the benefit of

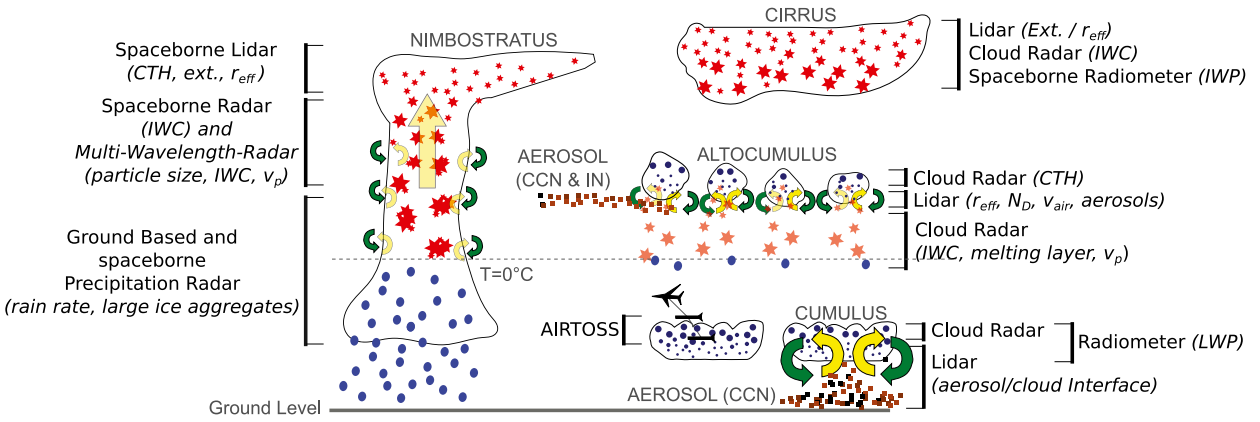

FIG. 10-3. Overview on remote sensing observation methods. For each cloud type, the height range is depicted that is optimal for the observation with ground and spaceborne lidar and radar systems and aircraft-tossed systems. The single systems (lidar, radar, microwave radiometer, and AIRTOSS) are explained in this section. Main properties of clouds derived from remote sensing measurements are cloud-top height (CTH), LWC/liquid water path (LWP), IWC, Doppler velocity of falling particles (v_p), optical extinction (ext.), effective radius (r_{eff}), and the number of cloud droplets (N_D).

synergistic measurements of lidar and cloud radar in order to complement aircraft measurements under conditions of low ice concentrations. Prominent examples of studies that employ combined approaches between aircraft ground-based observations are Shupe et al. (2013) and Westbrook and Illingworth (2013).

Figure 10-3 also highlights the importance of lidar and radar depolarization measurements for the identification and classification of ice particles. Depolarization in general is measured by emitting radiation in two perpendicular polarization states (dual-polarization method) or emitting in one polarization state and detecting in two. Dual-polarization methods have a long history for weather radars, because they can be used for the classification of hydrometeors (Thompson et al. 2014) or estimation of rain rates (Cifelli et al. 2011). Recently, dual-polarization methods for the size estimation of ice particles have also been implemented into cloud radars (Myagkov et al. 2016). Figure 10-4 shows an example of a synergistic measurement result obtained from lidar, cloud radar, and microwave radiometer processed with the Cloudnet algorithm, which provides—among others—liquid water content (LWC) and IWC (Hogan et al. 2006). The lidar primarily detects the bases of liquid cloud layers, but also some of the ice particles falling from the mixed-phase cloud layer. Lidar depolarization shows low values at cloud top, where liquid particles dominate and high values in the virga. Liquid water path in the cloud top is measured with a microwave radiometer and scaled to the geometric extent of the liquid cloud layer (Fig. 10-4g). Ice water content is calculated using the aircraft-derived parameterization of Hogan et al. (2006), which again highlights the powerful combination of ground-based remote sensing observations with aircraft in situ measurements.

Measurements as shown in Fig. 10-4 can be generated automatically by state-of-the-art synergistic algorithms. However, they can only provide an overview of the distribution of cloud particles and the height level of ice nucleation. The following evolution of a particle can be tracked using methods of fall-streak tracking (Marshall 1953). Hogan and Kew (2005) and Kalesse et al. (2016) showed how in situations when vertical wind shear is observed, the evolution of snow particles should be tracked along slanted fall streaks instead of considering vertical profiles. Other studies used the principle to observe hydrometeors with high spatial resolution (Collier 1999) or to improve radar-derived rainfall estimations (Mittermaier et al. 2004; Lack and Fox 2007; Lauri et al. 2012).

Kalesse et al. (2016) assumed that the ice-formation process is stationary during cloud observation, and only additional information about the horizontal wind field is needed in order to follow particles through a cloud. Observation of the complete life cycle of ice particles from the level of ice formation toward ground level, which is possible by such techniques, is important, for example, in order to discriminate between primary ice formation or particle generation triggered by cloud-seeding effects. Figure 10-5 shows an example of a fall streak tracked from the level of ice formation through a mixed-phase cloud system down to the ground where snowfall is detected. In this example, ice particles generated near the top of the deep cloud frontal system are falling through a supercooled liquid layer where they experience riming and new ice particle formation happens. The newly formed particles could either originate from ice multiplication (break up of rimed particles) or appear because of primary ice formation in the liquid layer (Zawadzki et al. 2001).

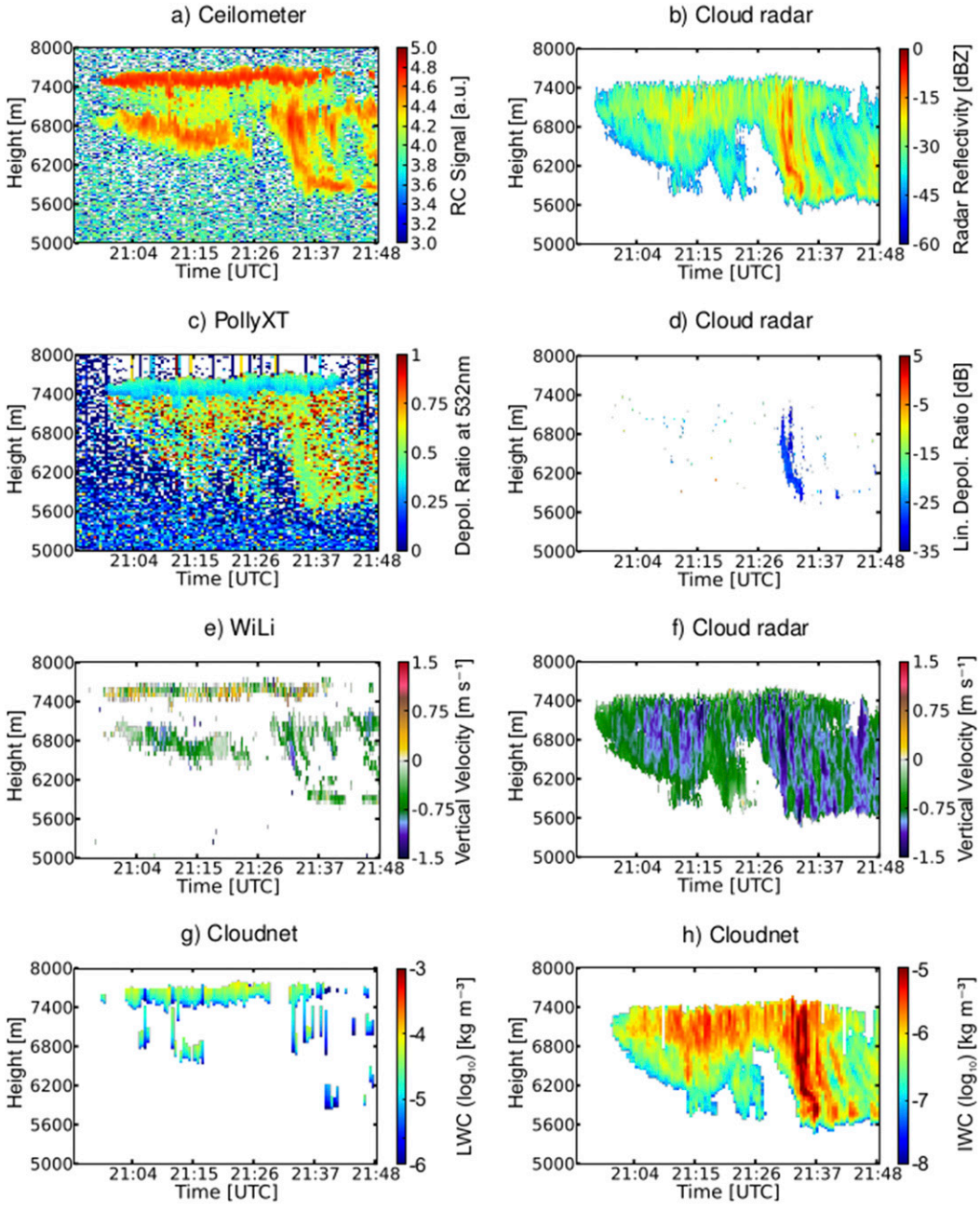

FIG. 10-4. Example of a combined lidar, cloud radar, and microwave radiometer measurement at Leipzig, Germany (2 Aug 2011): (a) lidar attenuated backscatter, (b) radar reflectivity factor, (c) lidar linear depolarization ratio, (d) cloud radar linear depolarization ratio, (e) vertical velocity from Doppler lidar, (f) vertical velocity from cloud radar, (g) LWC, and (h) IWC. Temperature at cloud top (7500 m) is −35°C.

Additionally, Fig. 10-5 highlights the information content of the full cloud radar Doppler spectrum. As emphasized in Kollias et al. (2007), spectral Doppler information is expected to be one of the main tools for future observational studies on cloud microphysical properties. Several previous studies have demonstrated the potential of using multimodal cloud radar Doppler spectra to characterize the liquid-phase and ice-phase components in mixed-phase clouds (e.g., Shupe et al. 2004; Luke et al. 2010; Jensen et al. 2010; Luke and Kollias 2013; Rambukkange et al. 2011; Verlinde et al. 2013; Kalesse et al. 2016). While lower moments of the radar spectrum (namely effective reflectivity Z_e and mean Doppler velocity) are highly sensitive to the

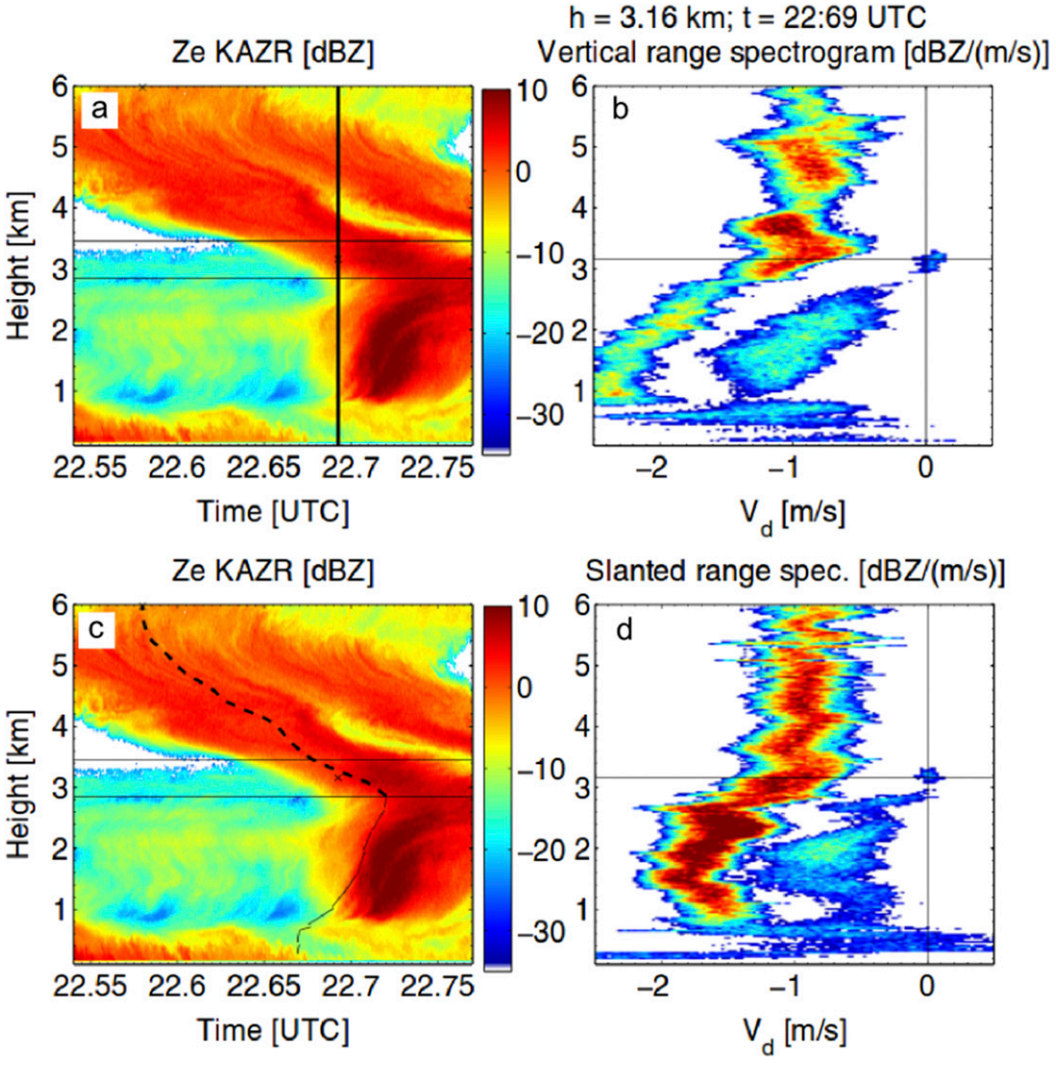

FIG. 10-5. (a), (c) The reflectivity field of a 35-GHz zenith-pointing cloud radar in a wintertime deep frontal system observed at 21 Feb 2014 in Finland. Thin horizontal lines indicate location of a supercooled liquid layer. (b) The Doppler velocity vs height spectrogram along the black vertical line in (a). (d) The range spectrogram along the slanted fall streak marked in (c). Figure from Kalesse et al. (2016).

largest particles in the cloud volume detected by radar (as mentioned before Z_e is proportional to D^6), considering the full Doppler spectrum enables detection of smaller particles with lower fall velocities. Doppler cloud radar observations with a high temporal and spectral resolution are required nevertheless, because the Doppler spectrum is also affected by dynamical effects such as turbulence, which lead to spectral broadening and hamper microphysical retrievals (Babb et al. 1999; Scott et al. 2001). However, if sufficiently resolved, the Doppler velocity of the liquid cloud particles can be used as vertical air motion tracer. This approach is based on the assumption that the terminal velocity of small cloud droplets can be neglected compared to typical vertical air motions in clouds (Kollias et al. 2001). As an alternative to the use of the full Doppler spectrum, the use of higher moments of the Doppler spectrum such as skewness and kurtosis as well as the slopes of the Doppler spectrum have been found useful for cloud observations (Luke and Kollias 2013; Maahn et al. 2015; Maahn and Löhnert 2017).

Recently, triple-frequency radar measurements in snowfall have the potential to give insight into ice particle characteristic size, habits, and ice particle density (Kneifel et al. 2014; Kulie et al. 2014). Kneifel et al. (2015) investigated relations between collocated ground-based triple-frequency radar observations (Ka, W, X band) in snowfall with in situ measurements performed at the ground. Concurrent analyses of two dual-wavelength ratios (i.e., the differences of the logarithmic effective radar

reflectivity factor at two radar frequencies) at X/Ka band and Ka/W band were made. Clear signatures of snow particles with different characteristic sizes and densities (e.g., large low-density aggregates and heavily rimed snowflakes) could be distinguished in the triple-frequency space and were validated by the in situ measurements. As a further step, Kneifel et al. (2016) for the first time analyzed triple-frequency radar Doppler spectra in snowfall and showed that such sophisticated observations can be used to validate snow scattering models.

c. *Spaceborne lidar and radar*

The *CloudSat* and *CALIPSO* satellites were launched in 2006 to join the A-Train, a polar satellite family currently consisting of six satellites in a sun-synchronous orbit that passes the equator at 1330 solar time and the ground track pattern repeats after approximately 16 days (Stephens et al. 2002). The Cloud Profiling Radar (CPR) aboard *CloudSat* and the Cloud–Aerosol Lidar with Orthogonal Polarization (CALIOP) aboard *CALIPSO* are the first combination of active radar and lidar instruments in orbit specifically designed to globally observe clouds and aerosols from space. The measured signals from CPR and CALIOP are proportional to the amount of microwave (CPR) and infrared (CALIOP) radiation scattered back from hydrometeors in the atmosphere. The CALIOP lidar operates at a wavelength of 1064 nm and is therefore sensitive to small particles, while CPR, with its operation at 94 GHz (3-mm wavelength), is rather sensitive to larger and precipitating particles. Hence, CALIOP detects the thin cirrus clouds and cloud tops, and CPR probes thicker clouds and precipitation (Sassen et al. 2008), which cannot be penetrated by lidar. Their synergistic observations are extensively used to study cloud formation and maintenance mechanisms (e.g., Hogan and Illingworth 1999; Sato and Okamoto 2006; Sassen et al. 2008; Grenier et al. 2009; Sassen et al. 2009; Sassen and Zhu 2009; Wu et al. 2009; Yoshida et al. 2010; Zhang et al. 2010; Stein et al. 2011; Del Genio et al. 2012; Bühl et al. 2013; Battaglia and Delanoë 2013).

Lidars suffer from attenuation by thick clouds, and because most lidars for aerosol and cloud detection are deployed on the ground (Pal et al. 1992; Van Tricht et al. 2014) their measurements can be obscured by low-level thick clouds (Thorsen et al. 2011). This problem is mitigated by CALIOP, which looks from above and is, therefore, well suited to retrieve cloud-top properties. In contrast to CALIOP, the *CloudSat* radar can even penetrate thick clouds. However, *CloudSat*'s CPR suffers from ground reflection that contaminates the observations near the ground (Marchand et al. 2008; Maahn et al. 2014). Measurements close to the ground are also challenging for vertically pointing ground-based radar systems because of detector saturation and other near-field effects (Görsdorf et al. 2015).

The raw power returns are converted into an equivalent attenuated reflectivity factor profile (CPR; Stephens et al. 2002) and attenuated backscatter profile (CALIOP; Winker et al. 2009). From these data products users can develop their own algorithms and products. Examples include the *CloudSat* radar–lidar geometrical profile product that provides vertical and spatial structure of hydrometeor layers based on combined *CloudSat*/*CALIPSO* observations (Mace and Zhang 2014), the Combined Radar and Lidar Cloud Scenario Classification Product that includes information on cloud phase of the detected hydrometeor layers (Delanoë and Hogan 2008; Mace and Zhang 2014), and multiple data products with retrieved ice and liquid water contents and cloud optical depths (Austin et al. 2009; Vaughan et al. 2009; Winker et al. 2009; Deng et al. 2010).[1]

Algorithms have been developed and refined to take advantage of the nearly coincident satellite lidar and radar observations and combine the strengths of both systems (e.g., Delanoë and Hogan 2010; Ceccaldi et al. 2013). Such data products provide vertically resolved profiles of cloud phase, and thus can be used to derive monthly cloud fraction data (Kay et al. 2008; Verlinden et al. 2011) and to determine aerosol–ice interactions and ice formation (Grenier et al. 2009). Furthermore, comparisons against ice microphysical observations made by ground-based systems from the tropics to the poles (Protat et al. 2009, 2010; Thorsen et al. 2011; Bromwich et al. 2012) can be performed. CALIOP data reveal the global cirrus cloud distribution (Sassen et al. 2008) and depolarization within ice clouds, with depolarization increasing at higher altitudes and decreasing with increasing latitude (Sassen and Zhu 2009).

Reconciling differences between climatologies of, for example, heterogeneous ice formation calculated from ground-based observations with the corresponding results from satellite-based instruments is necessary for validation of satellite data products (Seifert et al. 2010; Kanitz et al. 2011; Bühl et al. 2013). The accuracy of many datasets over parts of Earth, such as the Southern Ocean, remains questionable because of the lack of in situ measurements and the use of empirical relationships in the retrievals, which are derived from data in other locations. The correct representation of ice in weather forecasting and general circulation models remains challenging, with over- and underestimates

[1] Publicly accessible data repositories for *CloudSat* and *CALIPSO* can be found online at cloudsat.atmos.colostate.edu/data and www-calipso.larc.nasa.gov/.

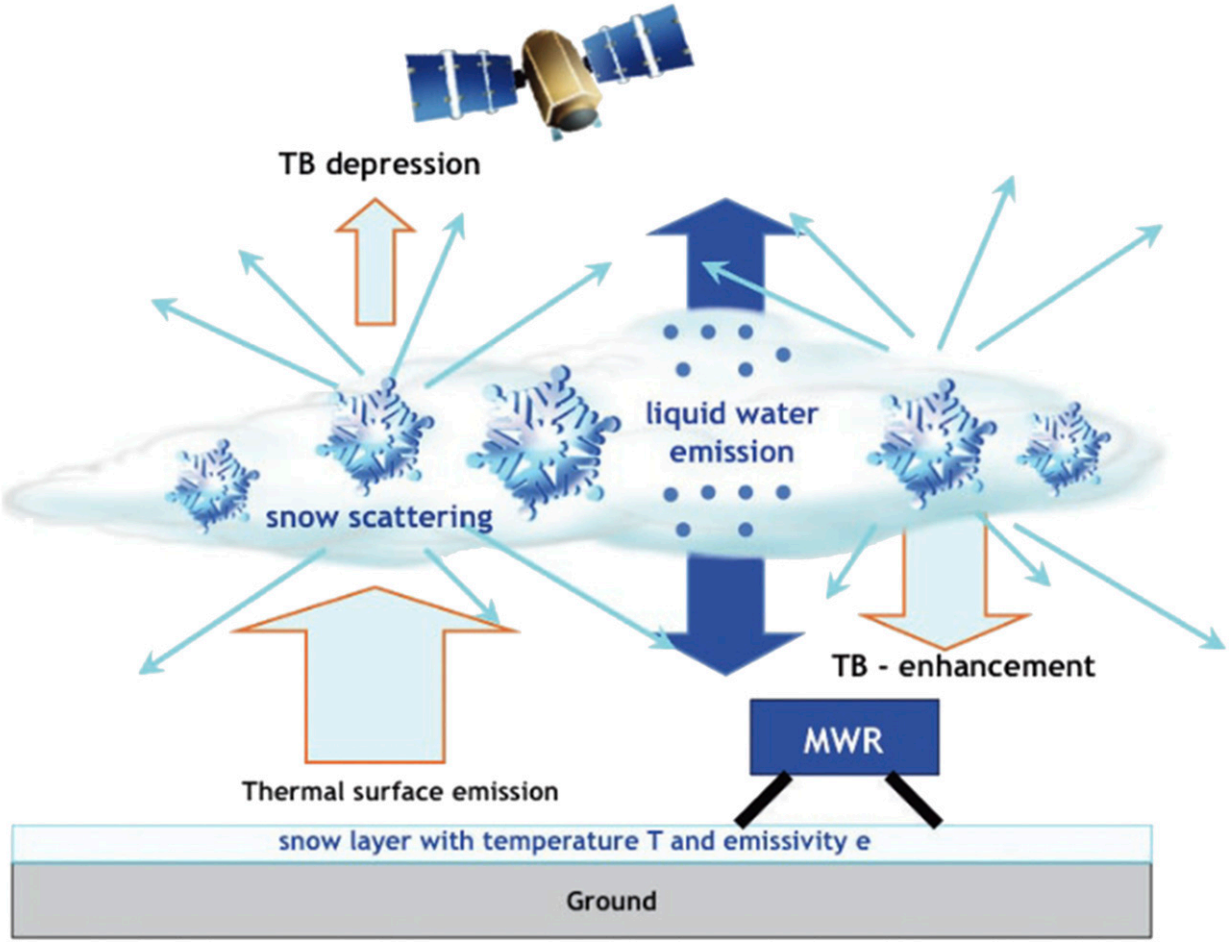

FIG. 10-6. Illustration of the effects of liquid water and snow crystals on microwave TB measured at surface level and from space. Figure from Löhnert et al. (2011).

of ice compared with *CALIPSO* and *CloudSat* observations in various regions of Earth and in different temperature regimes (Delanoë et al. 2011).

d. *Microwave radiometers for measurement of atmospheric ice water path*

Microwave radiometry makes use of the interaction of microwave radiation (between 1 and 1000 GHz) with atmospheric gases and particles. While brightness temperature (TB) measurements along absorption lines are used for profiling of temperature and gases, window regions give insight into clouds and precipitation as they are semitransparent in this spectral region (see, e.g., Petty 2006). In general, extinction by water vapor and hydrometeors increases with frequency, with the strongest effect for ice clouds. Their effect can be neglected for frequencies below 60 GHz, enabling the retrieval of the liquid water path from multispectral measurements. However, with higher frequencies, both scattering cross section and absorption cross section of ice particles strongly increase. The dominance of scattering leads to the fact that a layer of ice particles causes a TB depression for space-based observations because the thermal emission of the surface and lower atmospheric layers is scattered away (Fig. 10-6). This is the classical principle behind precipitation retrieval over land from millimeter-wave satellite observations (e.g., Grody 1991; Laviola and Levizzani 2011). For ground-based observations, however, scattering by ice particles leads to a brightness temperature increase, because the thermal emission of the relatively warm surface is scattered back to the radiometer.

The brightness temperature depression/increase (downward/upward pointing) is related to the integrated IWP (Evans et al. 1999, 2005; Kneifel et al. 2010). Because the interaction between ice particles and microwave radiation depends to first order on the relation between particle size and wavelength, it is important that the selected microwave frequencies are sensitive to the ice particle size distribution. In this respect, passive microwave observations fill the gap between infrared (smallest

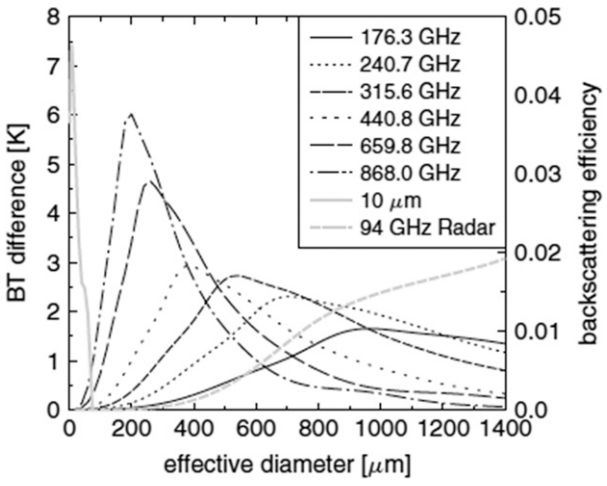

FIG. 10-7. The sensitivity of measurements at various frequencies to ice particle size. A fixed amount of cloud ice (IWP = 0.001 g m^{-2}) and a narrow size distributions with different D_{eff} have been used. For each D_{eff}, the difference between clear-sky and cloudy radiance is displayed. For comparison, the two gray curves show the size sensitivity for IR radiances at 10 μm (solid), and for radar backscatter measurements at 95 GHz (dashed). The right axis is for the radar curve, while the left axis is for all other curves. Figure from Buehler et al. (2007).

particles) and radar (Fig. 10-7). Frequencies below 200 GHz are, therefore, mainly suited to sense snow while higher frequencies, that is, submillimeter wavelengths, can be used to study ice clouds (Evans and Stephens 1995; Evans et al. 1999). However, not only ice scattering but also the continuum emission of liquid water and water vapor increases with frequency, which reduces the penetration depth with increasing frequencies. This is less of a problem for downward-pointing (satellite, high-flying aircraft) than upward-pointing geometries as the surface contribution is omitted. From satellites the strong difference in opacity along water absorption lines can be exploited to infer the medium altitude of the ice cloud, that is, the height where IWP has reached half of its column value (Jiménez et al. 2007).

Other ice particle properties like shape, density, and orientation also influence the microwave signal. For example, the preferentially horizontal orientation of snow particles (e.g., Pruppacher and Klett 1997) may cause a polarization difference (PD) of vertically and horizontally polarized brightness temperatures of more than 10 K for spaceborne observations (Gong and Wu 2017) and more than 8 K for ground-based observations (Xie et al. 2012) depending on aspect ratio. However, the strong absorption and emission of supercooled liquid water (SCLW) can mask PD for ground-based operations. For spaceborne operations, it instead depends on the geometry: if the SCLW is above oriented particles, PD is reduced, while if it is below the ice layer, PD is actually enhanced (Xie et al. 2015). Also the presence of a melting layer can lead to an increased PD (Galligani et al. 2013; Gong and Wu 2017). IWP retrievals for current microwave satellite instruments exploiting the ice scattering signals for frequencies up to 190 GHz have been developed by Sun and Weng (2012), among others, for the Special Sensor Microwave Imager/Sounder (SSM/IS) and Surussavadee and Staelin (2009) for the Advanced Microwave Sounding Unit (AMSU)/Microwave Humidity Sounder (MHS). The Global Precipitation Measurement (GPM; Hou et al. 2014) mission launched in 2014 aims to provide global spaceborne measurements of falling snow from both active and passive microwave measurements, which both show a sensitivity threshold of about 0.5–1.0 mm h^{-1} melted snow rate (Skofronick-Jackson et al. 2015). However, at these frequencies information is gathered mainly from snow particles (see Fig. 10-6) and the sensitivity to smaller particles typically found in ice clouds is low. Islam and Srivastava (2015) show how infrared observations, in this case High Resolution Infrared Radiation Sounder (HIRS), that are sensitive to much smaller particles complement the information of AMSU/MHS. Holl et al. (2014) developed the Synergistic Passive Atmospheric Retrieval Experiment-ICE (SPARE-ICE), which provides IWP combining Advanced Very High Resolution Radiometer (AVHRR) and MHS. They find a median fractional error between SPARE-ICE and *CloudSat* to be around a factor of 2, which is similar as the random error of *CloudSat* IWC and in situ measurements. The suitability of the submillimeter region for ice cloud retrievals has already been demonstrated using limb sounding instruments mainly devoted to stratospheric chemistry. Specifically, the Microwave Limb Sounder (MLS) (Waters et al. 2006) with channels at 240 and 640 GHz and the submillimeter radiometer (SMR) on board the *Odin* satellite (Murtagh et al. 2002) with channels between 500 and 650 GHz provide information on upper-tropospheric ice water content (Wu et al. 2008, Eriksson et al. 2014).

The gap in terms of global ice cloud and light snow climatologies will be closed by the Ice Cloud Imager (ICI) on MetOP-SG to be launched 2021 (Bergada et al. 2016). The ICI will carry channels featuring submillimeter frequencies ranging from 183 GHz up to 664 GHz with the frequencies 243 and 664 GHz featuring vertical and horizontal polarization. In addition to IWP, the ICI will also deliver the median mass equivalent sphere diameter and the median IWP altitude (Buehler et al. 2012). For process studies and prestudies for a satellite mission, airborne sensors such as Compact Scanning Submillimeter-Wave Imaging Radiometer (CoSSIR; Evans et al. 2005), Conical Scanning Millimeter-Wave Imaging Radiometer (CoSMIR; Wang et al. 2007), and International

Submillimetre Airborne Radiometer (ISMAR; Fox et al. 2014) have been developed. In contrast to satellites, airborne instruments such as CoSMIR can also operate upward looking, which allows for observations of ice clouds in front of the cold cosmic background without being limited because of tropospheric water vapor when flying in high altitudes.

Ground-based microwave observations of ice clouds and snow are limited to high-altitude (Löhnert et al. 2011) or high-latitude sites (Shupe et al. 2013) because of the strong continuum emission of water vapor at other sites. At these sites, observation frequencies of 90 and 150 GHz are typically used. IWP can be derived from the TB increase (Kneifel et al. 2010) and polarized measurements have been used to differentiate between mixed-phase and pure snowfall events and indicate the alignment of snow particles (Xie et al. 2012).

e. Passive remote sensing of cloud phase using solar spectral reflectivity

1) Airborne radiation instruments

To measure cloud reflectivity, airborne radiation instruments can be used, such as the Spectral Modular Airborne Radiation Instrument (SMART) albedometer developed by Wendisch et al. (2001) and improved by Bierwirth et al. (2009), or the Solar Spectral Flux Radiometer (SSFR; Pilewskie et al. 2003). An overview of further airborne spectral radiation instruments and other airborne instrumentation is given by Wendisch et al. (2013b) and Wendisch and Brenguier (2013). Several types of spectral radiance instruments are commonly used for ice identification measurements in clouds. On the one hand, pointing single-pixel spectrometers observe one pixel. On the other hand, multiangular imaging spectrometers observe fields of pixels of the clouds. However, compared to pointing, single-pixel spectrometers, the wavelength resolutions of imaging spectrometers are often reduced and the opening angle is different. Prominent examples of commercially available imaging spectrometers are the Eagle and Hawk [push broom line imager, up to 1024 spatial pixel (60°FOV), up to 1024 spectral pixel; see, e.g., Schäfer et al. (2015)], charge-coupled device (CCD) cameras (Ehrlich et al. 2012), and polarization cameras.

2) Ice identification using cloud-reflected radiation

Figure 10-8 illustrates the basic principle of a method widely used to identify the ice phase in clouds, see, for example, Pilewskie and Twomey (1987), Ehrlich et al. (2008), Wendisch and Ehrlich (2011), and Jäkel et al. (2013). Figure 10-8b shows the spectrum of the absorption index (imaginary part of refractive index n_i) for ice (red line) and liquid water (blue line), respectively. In particular, in parts of the near-infrared (NIR) wavelength region (≈1.4–1.9 μm) the maxima of the absorption indices are at different wavelengths, and the spectral slopes are also different. These spectral features are reproduced in examples of cloud reflectivity spectra (R_λ), shown in Fig. 10-8a. Cloud-reflected radiation spectra in the NIR exhibit a distinctly different slope as a function of the ice content in the cloud; see the red (ice) and blue (liquid water) lines in Fig. 10-8a. Consequently, the slope of the cloud reflectivity spectra can be used to identify ice in mixed-phase clouds. The spectral slope ice index I_S is defined as the relative spectral slope of the measured reflectivity R_λ at the two NIR wavelengths (λ = 1700 and 1640 nm): $I_S = (R_{1700} - R_{1640})/R_{1640}$. This ice index I_S has proven to be highly sensitive to spectral features of ice and liquid water absorption. From numerous simulations it is shown that values of $I_S < 20$ indicate a liquid water cloud, whereas $I_S \approx 30$ is representative for mixed-phase clouds, and larger values of I_S show the presence of ice clouds. A second ice index I_S utilizes a principal component analysis of the spectral reflectance in the same NIR wavelength range to distinguish ice and liquid water absorption in the measurements.

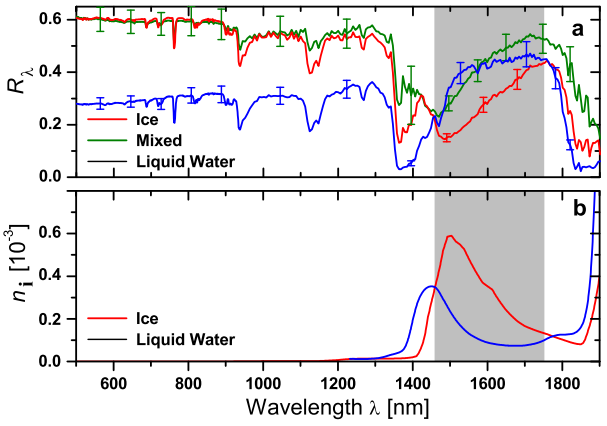

FIG. 10-8. (a) Spectra of solar reflectivity R for ice (red), mixed-phase (green), and liquid water (blue) clouds. The spectral range in which the spectral shapes are different is indicated by the gray areas. (b) Spectra of imaginary part of refractive index n_i for ice (red) and liquid water (blue). This figure is adapted from Ehrlich et al. (2008).

From the slope several realizations of ice indices can be derived that describe the phase composition of the cloud (Ehrlich et al. 2008). Unfortunately, no quantification of ice and liquid water content can be derived because of interferences with size and other parameters of the ice particles.

3) Application of ice index technique

Two example of ice index measurements are discussed: The first one results from pointing, single-pixel

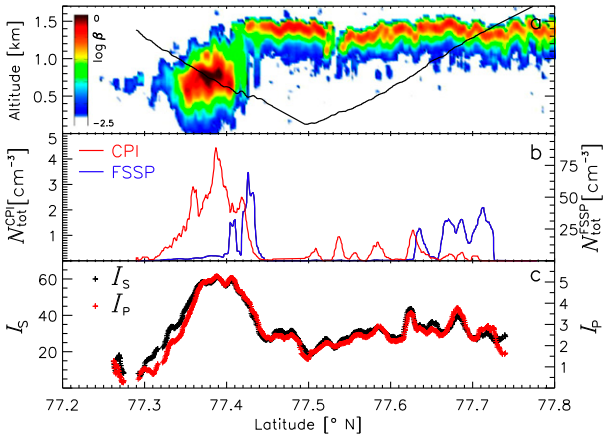

FIG. 10-9. Time series of different measurements obtained over mixed-phase clouds in the Arctic (see Ehrlich et al. 2008). (a) Profile of total attenuated backscatter coefficient β [sr^{-1} km^{-1}] measured by *CALIPSO* in a cloud observed on 7 Apr 2007. The flight track of the in situ measurements is overlaid as a black line. (b) Ice and liquid water particle concentrations N_{tot} measured by CPI (red) and Forward Scattering Spectrometer Probe (FSSP) (blue) along the flight track and (c) the ice indices for the same positions.

spectrometer measurements conducted above Arctic low-level clouds (Ehrlich et al. 2008); the second one stems from imaging spectrometer measurements of deep convective clouds in Amazonia (Wendisch et al. 2016).

Ehrlich et al. (2008) calculated different realizations of the ice index from spectral reflectivity measurements conducted over Arctic low-level clouds (see Fig. 10-9). The two indices I_S and I_P are derived from two techniques described in more detail by Ehrlich et al. (2008). While I_S analyzes the spectral slope of the reflectance in the NIR wavelength range, I_P utilizes a principal component analysis (PCA) of the spectral reflectance. Figure 10-9c shows a time series of two of the derived ice indices I_S and I_P. Both ice indices show a similar relative course, the maximum coincides with a region where in situ measurements [Fig. 10-9b; cloud particle imager (CPI)] and lidar data (Fig. 10-9a) also indicate ice in the respective cloud portion. Furthermore, all three methods (ice index, in situ data, lidar) show a similar temporal evolution for mixed-phase clouds. The lidar profiles reveal that in the southern part of the cloud (left side of Fig. 10-9) ice particles are precipitating down to the surface. These precipitation particles, which are also observed from *CloudSat* (reflectivity) and can be detected by the lidar because they are not capped by a liquid water layer in this area.

Wendisch et al. (2016) observed deep convective clouds over Amazonia by a side-viewing technique instead of looking from above at the cloud top (see Fig. 10-10) during the Aerosol, Cloud, Precipitation, and Radiation Interactions and Dynamics of Convective Cloud Systems–Cloud Processes of the Main Precipitation Systems in Brazil: A Contribution to Cloud Resolving Modeling and to the GPM (ACRIDICON-CHUVA) campaign. In this case an imaging spectrometer was installed inside the aircraft. The aircraft flies by (orbits) the cloud to obtain vertical profiles of the ice index. In Fig. 10-11, the NIR ice indices have been calculated from the spectra of the reflected radiation. Figure 10-11a shows the two-dimensional plots, Fig. 11b illustrates averages over the scene with indications of the height of the mixing layer. These measurements have been collected to obtain statistical data of the thickness and altitude of the mixed-phase layer in deep convective clouds and their dependence on aerosol and meteorological conditions (for details, please see Wendisch et al. 2016).

4) COLLOCATED MEASUREMENT STRATEGY

For a validation of the phase identification technique described above, collocated measurements of solar spectral radiation reflected by the clouds and concurrent in situ measurements of the cloud microphysics are ideal. Here two approaches are introduced: helicopterborne (Werner et al. 2013, 2014) and aircraftborne (Frey et al. 2009; Finger et al. 2016). Figure 10-12 illustrates both approaches. For low clouds a slow-flying helicopter is used as an instrument carrier for Spectral Modular Airborne Radiation measurement system (SMART-HELIOS) and Airborne Cloud Turbulence Observation System (ACTOS) payloads. SMART-HELIOS takes spectral cloud reflectivity measurements from above the cloud to remotely sense the cloud ice; ACTOS does the microphysical cloud sampling to indicate the cloud ice with in situ measurements inside the cloud. For high ice clouds, a fast-flying jet aircraft is used in combination with a towed measurement platform [Airborne Towed Sensor Shuttle (AIRTOSS)]. In this case the remote sensing of the ice in the clouds is done by spectral reflectivity measurements on board the aircraft; the in situ verification is done by the AIRTOSS, which, by the way, contains not only a cloud microphysical in situ probe but also upward- and downward-looking solar spectral radiometers.

These collocated measurements have proven to be extremely valuable not only to verify remote sensing techniques to detect ice in clouds, but also to conduct studies of aerosol indirect radiative effects on cloud properties (Werner et al. 2014) and to perform collocated radiative budget measurements of clouds (Finger et al. 2016). But even if aircraft and in situ measurements are not collocated, they can be combined statistically:

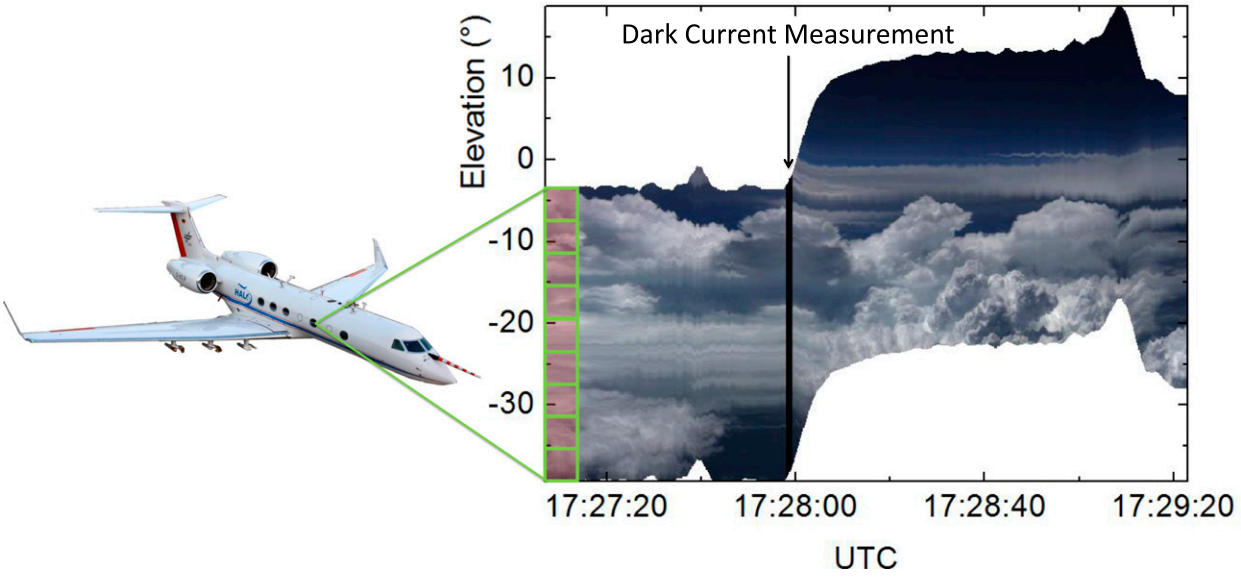

FIG. 10-10. Cloud-side observations of reflected solar radiances for a cloud. Changes of the elevation angle above/below horizon results from variable roll angles of the aircraft.

Maahn et al. (2015) used the radar-derived relation between radar reflectivity and mean Doppler velocity together with aircraft in situ measurements in order to estimate the mass–size relation of arctic ice clouds as a function of temperature.

3. Conclusions and outlook

Active remotes sensing sensors like ground-based and spaceborne lidars and radars deliver direct information about the process of ice formation. It has been shown that combined approaches—for example, aircraft combined with active or passive remote sensing—can deliver a wealth of information. Passive optical observations at cloud top with high resolution especially can provide instant information about the radiative properties of a cloud, directly connecting the process level and the climatological impact. Methods like fall-streak tracking introduce a time component and allow tracing back the ice particles to their common point of origin.

The largest differences between ground-based and spaceborne systems are the scales that can be resolved in clouds; for example, ground-based cloud radars can resolve about 50 m horizontally, and spaceborne radars

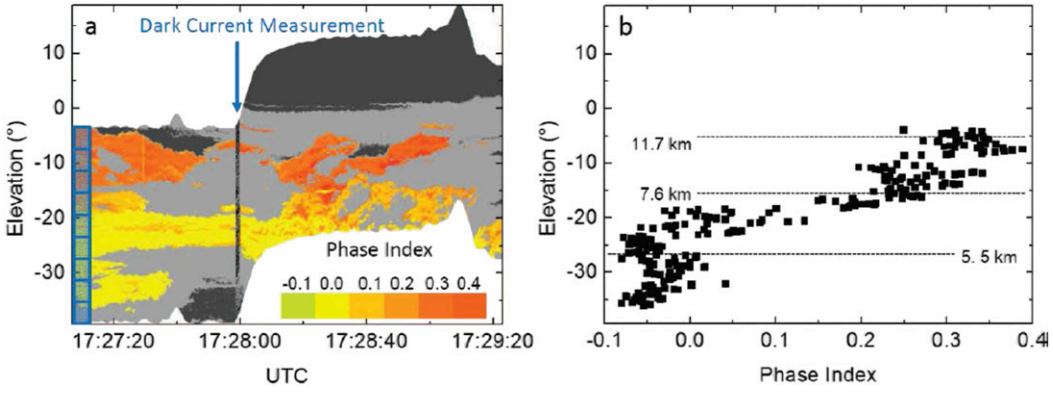

FIG. 10-11. Phase index derived from measurements of cloud-side reflected radiances for an example cloud. (a) Time series of vertical distribution of the phase index (side view), recorded during a flyby. The different colors represent values of the phase index. The dark gray areas indicate cloudless portions or land surface; the light gray areas represent shadow zones of the cloud sides, which are excluded from further analysis by an automatic cloud mask algorithm. These shadowed areas are not suitable for phase index analysis. The black vertical line indicates a dark-current measurement. (b) Vertical profile of phase index; three approximate altitudes (5.5, 7.6, and 11.7 km) are allocated to vertical pixels.

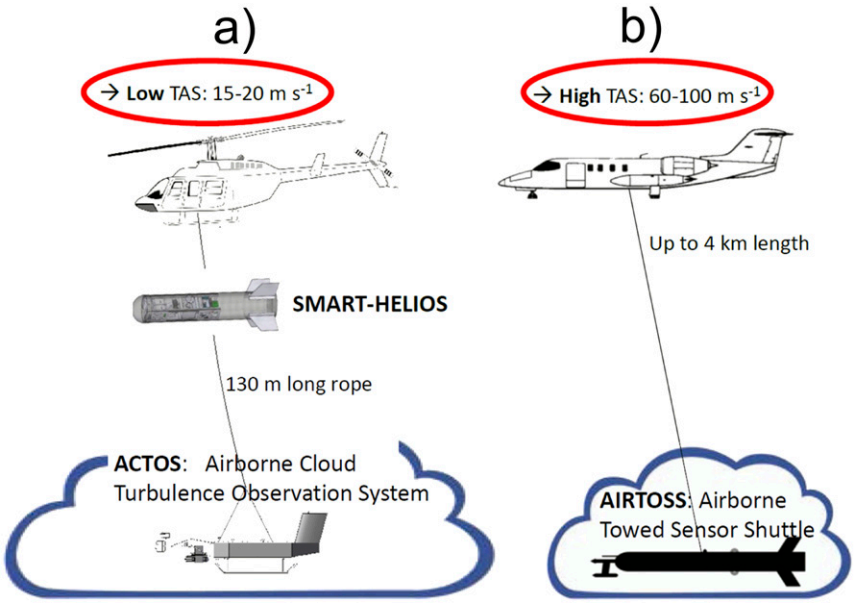

FIG. 10-12. Two strategies for collocated radiation and microphysical cloud measurements are shown: (a) helicopter based and (b) aircraft based.

can resolve about 1000 m. Active ground-based systems can hence usually resolve the process length scales even of thin clouds (<300 m), while spaceborne systems still can, for example, observe the resulting ice mass. Recent developments of imaging systems spanning the infrared to ultraviolet wavelength range are about to go below the limit of 1000-m resolution (Cao et al. 2014). Such spaceborne measurements can provide a basic set of measurement variables that then can be used to infer indirect information about cloud processes via detailed modeling (Rosenfeld et al. 2014). Table 10-2 summarizes the advantages and disadvantages of the measurement systems described in this chapter and shows how passive and active optical and microwave observation systems complement each other, in spite of their differences.

From Fig. 10-2, it seems as if there was a global coverage of remote sensing measurement campaigns, dedicated to ice formation. However, continuous long-term measurements are limited to a small band in the Northern Hemisphere with strong accumulations in central Europe and central North America. The distribution of activities in the figure poses the question: Where to go next? There are obviously huge gaps in the global coverage of continuous active remote sensing measurements. However, such measurements are vital, for example, for the validation and ground truthing of combined remote sensing satellite missions (Illingworth et al. 2015). Also, the operational study of ice-formation processes is restricted to the meteorological characteristics of the northern midlatitudes, and there might be important variations on a regional scale. It becomes very clear that efforts have to be taken in order to enable continuous high-quality measurements also in regions of Earth that are less privileged. Efforts like the activities mentioned in Fig. 10-2 that took place, for example, at Manus, Nauru, northern Africa, or the central Amazonian rain forest have already gone into this direction. Such efforts should not be restricted to short-term campaign-like activities but should encompass long-term involvements in order to build up sustainable infrastructure on site.

It appears as if the impact of single instrument observations has diminished and the future of remote sensing research is built through synergistic multi-instrument and multiplatform approaches. The use of different methodologies (e.g., combinations of radar and lidar or in situ and remote sensing observations) allows for compensation of the limitations of a single measurement platform. Recently, scanning techniques with multiple radar instruments have been used to provide three-dimensional insight into cloud systems (Kollias et al. 2014) and multiwavelength techniques have become operationally applicable (Kneifel et al. 2011). For zenith-pointing radars, the use of the full Doppler spectrum opens new possibilities (Kollias et al. 2007). Lidars deliver more and more quantitative information about small cloud particles like cloud droplets (Donovan et al. 2015) or aerosol particles (Mamouri and Ansmann 2015), which are precursors for heterogeneous ice formation.

TABLE 10-2. Overview about strengths and weaknesses of the measurement systems.

System	Known strengths	Known weaknesses
Satellite lidar and radar	Near-global coverage by the same sensors; high-altitude top-down observations	No observations at high latitudes (''pole hole'')
	Vertically resolved information	Limited temporal resolution
	Lidar–radar synergy	Ground clutter (*CloudSat*)
	Excellent cloud-top information from CALIOP	Narrow swath
		Often no cloud-base information from CALIOP because of attenuation of the signal
Microwave radiometers	Microwave radiation can penetrate optically thick clouds	SCLW can superimpose signals of ice
	Integral signal with lower size sensitivity compared to radar	No profiling abilities
	Particle orientation causes PD	Ice scattering properties challenging
	Satellites can provide global products for IWP	Poor spatial resolution
Passive sensors	Lightweight	Nonspherical shapes (cirrus) (Eichler et al. 2009)
	Portable	Multilayer clouds (Werner et al. 2013)
	Broadband/wide angle	Cloud inhomogeneity effects (Schmidt et al. 2010; Werner et al. 2014)
		Sea ice and snow surfaces (Schäfer et al. 2015)
		Reflection–transmission (Brückner et al. 2014)
Ground-based lidar	Aerosol detection	Strong attenuation in liquid layers
	Detection of liquid layers	Limited operation capabilities in precipitation
Ground-based radar	Suitable for detection and detailed analysis of large particles	Detection of liquid layers difficult
	Can penetrate thick clouds and precipitation	Signal dominated by largest particles in observation volume
	Can measure sedimentation velocity	
	Spectrum reveals information about particle size distribution	

Acknowledgments. We gratefully acknowledge the support from the Transregional Collaborative Research Center (TR 172) Arctic Amplification: Climate Relevant Atmospheric and Surface Processes, and Feedback Mechanisms (AC)^3, which is funded by the German Research Foundation (DFG, Deutsche Forschungsgemeinschaft). In addition, the authors would like to thank the many sponsors who have provided funding for the monograph: Leibniz Institute for Tropospheric Research (TROPOS), Forschungszentrum Jülich (FZJ), and Deutsches Zentrum für Luft- und Raumfahrt (DLR), Germany; ETH Zurich, Switzerland; National Center for Atmospheric Research (NCAR), United States; the Met Office, United Kingdom; the University of Illinois, United States; Environment and Climate Change Canada (ECCC), Canada; National Science Foundation (NSF), AGS 1723548, National Aeronautics and Space Administration (NASA), United States; the International Commission on Clouds and Precipitation (ICCP), the European Facility for Airborne Research (EUFAR), and Droplet Measurement Technologies (DMT), United States. NCAR is sponsored by the NSF. Any opinions, findings, and conclusions or recommendations expressed in this publication are those of the author(s) and do not necessarily reflect the views of the National Science Foundation.

REFERENCES

Anderson, T., and Coauthors, 2005: An ''A-Train'' strategy for quantifying direct climate forcing by anthropogenic aerosols. *Bull. Amer. Meteor. Soc.*, **86**, 1795–1809, doi:10.1175/BAMS-86-12-1795.

Ansmann, A., R. Engelmann, D. Althausen, U. Wandinger, M. Hu, Y. Zhang, and Q. He, 2005: High aerosol load over the Pearl River Delta, China, observed with Raman lidar and sun photometer. *Geophys. Res. Lett.*, **32**, L13815, doi:10.1029/2005GL023094.

——, H. Baars, M. Tesche, D. Müller, D. Althausen, R. Engelmann, T. Pauliquevis, and P. Artaxo, 2009a: Dust and smoke transport from Africa to South America: Lidar profiling over Cape Verde and the Amazon rainforest. *Geophys. Res. Lett.*, **36**, L11802, doi:10.1029/2009GL037923.

——, and Coauthors, 2009b: Evolution of the ice phase in tropical altocumulus: SAMUM lidar observations over Cape Verde. *J. Geophys. Res.*, **114**, D17208, doi:10.1029/2008JD011659.

Austin, R. T., A. J. Heymsfield, and G. L. Stephens, 2009: Retrieval of ice cloud microphysical parameters using the CloudSat millimeter-wave radar and temperature. *J. Geophys. Res.*, **114**, D00A23, doi:10.1029/2008JD010049.

Babb, D. M., J. Verlinde, and B. A. Albrecht, 1999: Retrieval of cloud microphysical parameters from 94-GHz radar Doppler power spectra. *J. Atmos. Oceanic Technol.*, **16**, 489–503, doi:10.1175/1520-0426(1999)016<0489:ROCMPF>2.0.CO;2.

Battaglia, A., and J. Delanoë, 2013: Synergies and complementarities of CloudSat-CALIPSO snow observations. *J. Geophys. Res. Atmos.*, **118**, 721–731, doi:10.1029/2012JD018092.

Bergada, M., and Coauthors, 2016: The Ice Cloud Imager (ICI) preliminary design and performance. *14th Specialist Meeting*

on Microwave Radiometry and Remote Sensing of the Environment (MicroRad), Espoo, Finland, IEEE, doi:10.1109/MICRORAD.2016.7530498.

Bierwirth, E., and Coauthors, 2009: Spectral surface albedo over Morocco and its impact on radiative forcing of Saharan dust. *Tellus*, **61B**, 252–269, doi:10.1111/j.1600-0889.2008.00395.x.

Bodas-Salcedo, A., and Coauthors, 2014: Origins of the solar radiation biases over the Southern Ocean in CFMIP2 models. *J. Climate*, **27**, 41–56, doi:10.1175/JCLI-D-13-00169.1.

Bromwich, D. H., and Coauthors, 2012: Tropospheric clouds in Antarctica. *Rev. Geophys.*, **50**, RG1004, doi:10.1029/2011RG000363.

Brückner, M., A. Pospichal, A. Macke, and M. Wendisch, 2014: A new multispectral cloud retrieval method for ship-based solar transmissivity measurements. *J. Geophys. Res. Atmos.*, **119**, 11 338–11 354, doi:10.1002/2014JD021775.

Buehler, S. A., and Coauthors, 2007: A concept for a satellite mission to measure cloud ice water path, ice particle size, and cloud altitude. *Quart. J. Roy. Meteor. Soc.*, **133**, 109–128, doi:10.1002/qj.143.

——, and Coauthors, 2012: Observing ice clouds in the submillimeter spectral range: The CloudIce mission proposal for ESA's Earth Explorer 8. *Atmos. Meas. Tech.*, **5**, 1529–1549, doi:10.5194/amt-5-1529-2012.

Bühl, J., A. Ansmann, P. Seifert, H. Baars, and R. Engelmann, 2013: Toward a quantitative characterization of heterogeneous ice formation with lidar/radar: Comparison of CALIPSO/CloudSat with ground-based observations. *Geophys. Res. Lett.*, **40**, 4404–4408, doi:10.1002/grl.50792.

——, P. Seifert, A. Myagkov, and A. Ansmann, 2016: Measuring ice- and liquid-water properties in mixed-phase cloud layers at the Leipzig Cloudnet station. *Atmos. Chem. Phys.*, **16**, 10 609–10 620, doi:10.5194/acp-16-10609-2016.

Cao, C., S. Blonski, W. Wang, X. Shao, T. Choi, Y. Bai, and X. Xiong, 2014: Overview of Suomi NPP VIIRS performance in the last 2.5 years. *Earth Observing Missions and Sensors: Development, Implementation, and Characterization III*, X. Xiong and H. Shimoda, Eds., International Society for Optical Engineering (SPIE Proceedings, Vol. 9264), 926402, doi:10.1117/12.2068991.

Ceccaldi, M., J. Delanoë, R. J. Hogan, N. L. Pounder, A. Protat, and J. Pelon, 2013: From CloudSat-CALIPSO to EarthCare: Evolution of the DARDAR cloud classification and its comparison to airborne radar-lidar observations. *J. Geophys. Res. Atmos.*, **118**, 7962–7981, doi:10.1002/jgrd.50579.

Cifelli, R., V. Chandrasekar, S. Lim, P. C. Kennedy, Y. Wang, and S. A. Rutledge, 2011: A new dual-polarization radar rainfall algorithm: Application in Colorado precipitation events. *J. Atmos. Oceanic Technol.*, **28**, 352–364, doi:10.1175/2010JTECHA1488.1.

Cohen, J., and Coauthors, 2014: Recent Arctic amplification and extreme mid-latitude weather. *Nat. Geosci.*, **7**, 627–637, doi:10.1038/ngeo2234.

Collier, C. G., 1999: The impact of wind drift on the utility of very high spatial resolution radar data over urban areas. *Phys. Chem. Earth*, **24B**, 889–893, doi:10.1016/S1464-1909(99)00099-4.

Delanoë, J., and R. J. Hogan, 2008: A variational scheme for retrieving ice cloud properties from combined radar, lidar, and infrared radiometer. *J. Geophys. Res.*, **113**, D07204, doi:10.1029/2007JD009000.

——, and ——, 2010: Combined CloudSat-CALIPSO-MODIS retrievals of the properties of ice clouds. *J. Geophys. Res.*, **115**, D00H29, doi:10.1029/2009JD012346.

——, ——, R. M. Forbes, A. Bodas-Salcedo, and T. H. M. Stein, 2011: Evaluation of ice cloud representation in the ECMWF and Met Office models using CloudSat and CALIPSO data. *Quart. J. Roy. Meteor. Soc.*, **137**, 2064–2078, doi:10.1002/qj.882.

Del Genio, A. D., Y. Chen, D. Kim, and M.-S. Yao, 2012: The MJO transition from shallow to deep convection in *CloudSat*/CALIPSO data and GISS GCM simulations. *J. Climate*, **25**, 3755–3770, doi:10.1175/JCLI-D-11-00384.1.

Deng, M., G. G. Mace, Z. Wang, and H. Okamoto, 2010: Tropical Composition, Cloud and Climate Coupling Experiment validation for cirrus cloud profiling retrieval using CloudSat radar and CALIPSO lidar. *J. Geophys. Res.*, **115**, D00J15, doi:10.1029/2009JD013104.

Donovan, D. P., H. Klein Baltink, J. S. Henzing, S. R. De Roode, and A. P. Siebesma, 2015: A depolarisation lidar-based method for the determination of liquid-cloud microphysical properties. *Atmos. Meas. Tech.*, **8**, doi:10.5194/amt-8-237-2015.

Draine, B. T., and P. J. Flatau, 1994: Discrete-dipole approximation for scattering calculations. *J. Opt. Soc. Amer.*, **11A**, 1491, doi:10.1364/JOSAA.11.001491.

Ehrlich, A., E. Bierwirth, M. Wendisch, J.-F. Gayet, G. Mioche, A. Lampert, and J. Heintzenberg, 2008: Cloud phase identification of Arctic boundary-layer clouds from airborne spectral reflection measurements: Test of three approaches. *Atmos. Chem. Phys.*, **8**, 7493–7505, doi:10.5194/acp-8-7493-2008.

——, ——, ——, A. Herber, and J.-F. Gayet, 2012: Airborne hyperspectral observations of surface and cloud directional reflectivity using a commercial digital camera. *Atmos. Chem. Phys.*, **12**, 3493–3510, doi:10.5194/acp-12-3493-2012.

Eichler, H., A. Ehrlich, M. Wendisch, G. Mioche, J.-F. Gayet, M. Wirth, C. Emde, and A. Minikin, 2009: Influence of ice crystal shape on retrieval of cirrus optical thickness and effective radius: A case study. *J. Geophys. Res.*, **114**, D19203, doi:10.1029/2009JD012215.

Eriksson, P., B. Rydberg, H. Sagawa, M. S. Johnston, and Y. Kasai, 2014: Overview and sample applications of SMILES and Odin-SMR retrievals of upper tropospheric humidity and cloud ice mass. *Atmos. Chem. Phys.*, **14**, 12 613–12 629, doi:10.5194/acp-14-12613-2014.

Evans, K. F., and G. L. Stephens, 1995: Microwave radiative transfer through clouds composed of realistically shaped ice crystals. Part I. Single scattering properties. *J. Atmos. Sci.*, **52**, 2041–2057, doi:10.1175/1520-0469(1995)052<2041:MRTTCC>2.0.CO;2.

——, A. H. Evans, I. G. Nolt, and B. T. Marshall, 1999: The prospect for remote sensing of cirrus clouds with a submillimeter-wave spectrometer. *J. Appl. Meteor.*, **38**, 514–525, doi:10.1175/1520-0450(1999)038<0514:TPFRSO>2.0.CO;2.

——, J. R. Wang, P. E. Racette, G. Heymsfield, and L. Li, 2005: Ice cloud retrievals and analysis with the compact scanning submillimeter imaging radiometer and the cloud radar system during CRYSTAL FACE. *J. Appl. Meteor.*, **44**, 839–859, doi:10.1175/JAM2250.1.

Fan, J., Y. Wang, D. Rosenfeld, and X. Liu, 2016: Review of aerosol–cloud interactions: Mechanisms, significance, and challenges. *J. Atmos. Sci.*, **73**, 4221–4252, doi:10.1175/JAS-D-16-0037.1.

Finger, F., and Coauthors, 2016: Spectral optical layer properties of cirrus from collocated airborne measurements and simulations. *Atmos. Chem. Phys.*, **16**, 7681–7693, doi:10.5194/acp-16-7681-2016.

Fleishauer, R. P., V. E. Larson, and T. H. Vonder Haar, 2002: Observed microphysical structure of midlevel, mixed-phase clouds. *J. Atmos. Sci.*, **59**, 1779–1804, doi:10.1175/1520-0469(2002)059<1779:OMSOMM>2.0.CO;2.

Fox, S., C. K. Lee, I. Rule, R. King, S. Rogers, C. Harlow, and A. Baran, 2014: ISMAR: A new submillimeter airborne radiometer. *13th Specialist Meeting on Microwave Radiometry and Remote Sensing of the Environment (MicroRad)*, Pasadena, CA, IEEE, 128–132, doi:10.1109/MicroRad.2014.6878923.

Frey, W., H. Eichler, M. de Reus, R. Maser, M. Wendisch, and S. Borrmann, 2009: A new airborne tandem platform for collocated measurements of microphysical cloud and radiation properties. *Atmos. Meas. Tech.*, **2**, 147–158, doi:10.5194/amt-2-147-2009.

Galligani, V. S., C. Prigent, E. Defer, C. Jimenez, and P. Eriksson, 2013: The impact of the melting layer on the passive microwave cloud scattering signal observed from satellites: A study using TRMM microwave passive and active measurements. *J. Geophys. Res. Atmos.*, **118**, 5667–5678, doi:10.1002/jgrd.50431.

Gong, J., and D. L. Wu, 2017: Microphysical properties of frozen particles inferred from Global Precipitation Measurement (GPM) Microwave Imager (GMI) polarimetric measurements. *Atmos. Chem. Phys.*, **17**, 2741–2757, doi:10.5194/acp-17-2741-2017.

Gorodetskaya, I. V., and Coauthors, 2015: Cloud and precipitation properties from ground-based remote-sensing instruments in East Antarctica. *Cryosphere*, **9**, 285–304, doi:10.5194/tc-9-285-2015.

Görsdorf, U., V. Lehmann, M. Bauer-Pfundstein, G. Peters, D. Vavriv, V. Vinogradov, and V. Volkov, 2015: A 35-GHz polarimetric Doppler radar for long-term observations of cloud parameters—Description of system and data processing. *J. Atmos. Oceanic Technol.*, **32**, 675–690, doi:10.1175/JTECH-D-14-00066.1.

Grenier, P., J. Blanchet, and R. Muñoz-Alpizar, 2009: Study of polar thin ice clouds and aerosols seen by CloudSat and CALIPSO during midwinter 2007. *J. Geophys. Res.*, **114**, D09201, doi:10.1029/2008JD010927.

Grody, N. C., 1991: Classification of snow cover and precipitation using the special sensor microwave imager. *J. Geophys. Res.*, **96**, 7423–7435, doi:10.1029/91JD00045.

Heintzenberg, J., 2009: The SAMUM-1 experiment over Southern Morocco: Overview and introduction. *Tellus*, **61B**, 2–11, doi:10.1111/j.1600-0889.2008.00403.x.

Heymsfield, A. J., P. R. Field, M. Bailey, D. Rogers, J. Stith, C. Twohy, Z. Wang, and S. Haimov, 2011: Ice in Clouds Experiment—Layer Clouds. Part I: Ice growth rates derived from lenticular wave cloud penetrations. *J. Atmos. Sci.*, **68**, 2628–2654, doi:10.1175/JAS-D-11-025.1.

Hogan, R. J., and A. J. Illingworth, 1999: The potential of spaceborne dual-wavelength radar to make global measurements of cirrus clouds. *J. Atmos. Oceanic Technol.*, **16**, 518–531, doi:10.1175/1520-0426(1999)016<0518:TPOSDW>2.0.CO;2.

——, and S. F. Kew, 2005: A 3D stochastic cloud model for investigating the radiative properties of inhomogeneous cirrus clouds. *Quart. J. Roy. Meteor. Soc.*, **131**, 2585–2608, doi:10.1256/qj.04.144.

——, and C. D. Westbrook, 2014: Equation for the microwave backscatter cross section of aggregate snowflakes using the self-similar Rayleigh–Gans approximation. *J. Atmos. Sci.*, **71**, 3292–3301, doi:10.1175/JAS-D-13-0347.1.

——, M. P. Mittermaier, and A. J. Illingworth, 2006: The retrieval of ice water content from radar reflectivity factor and temperature and its use in evaluating a mesoscale model. *J. Appl. Meteor. Climatol.*, **45**, 301–317, doi:10.1175/JAM2340.1.

Holl, G., S. Eliasson, J. Mendrok, and S. A. Buehler, 2014: SPARE-ICE: Synergistic ice water path from passive operational sensors. *J. Geophys. Res. Atmos.*, **119**, 1504–1523, doi:10.1002/2013JD020759.

Hou, A. Y., and Coauthors, 2014: The Global Precipitation Measurement Mission. *Bull. Amer. Meteor. Soc.*, **95**, 701–722, doi:10.1175/BAMS-D-13-00164.1.

Huang, Y., C. N. Franklin, S. T. Siems, M. J. Manton, T. Chubb, A. Lock, S. Alexander, and A. Klekociuk, 2015: Evaluation of boundary-layer cloud forecasts over the Southern Ocean in a limited-area numerical weather prediction system using in situ, space-borne and ground-based observations. *Quart. J. Roy. Meteor. Soc.*, **141**, 2259–2276, doi:10.1002/qj.2519.

Illingworth, A. J., and Coauthors, 2007: Cloudnet: Continuous evaluation of cloud profiles in seven operational models using ground-based observations. *Bull. Amer. Meteor. Soc.*, **88**, 883, doi:10.1175/BAMS-88-6-883.

——, and Coauthors, 2015: The EarthCARE satellite: The next step forward in global measurements of clouds, aerosols, precipitation, and radiation. *Bull. Amer. Meteor. Soc.*, **96**, 1311–1332, doi:10.1175/BAMS-D-12-00227.1.

Islam, T., and P. K. Srivastava, 2015: Synergistic multi-sensor and multi-frequency retrieval of cloud ice water path constrained by CloudSat collocations. *J. Quant. Spectrosc. Radiat. Transfer*, **161**, 21–34, doi:10.1016/j.jqsrt.2015.03.022.

Jäkel, E., J. Walter, and M. Wendisch, 2013: Thermodynamic phase retrieval of convective clouds: Impact of sensor viewing geometry and vertical distribution of cloud properties. *Atmos. Meas. Tech.*, **6**, 539–547, doi:10.5194/amt-6-539-2013.

Jensen, E. J., L. Pfister, T. P. Bui, P. Lawson, and D. Baumgardner, 2010: Ice nucleation and cloud microphysical properties in tropical tropopause layer cirrus. *Atmos. Chem. Phys.*, **10**, 1369–1384, doi:10.5194/acp-10-1369-2010.

Jiménez, C., S. A. Buehler, B. Rydberg, P. Eriksson, and K. F. Evans, 2007: Performance simulations for a submillimeter-wave satellite instrument to measure cloud ice. *Quart. J. Roy. Meteor. Soc.*, **133**, 129–149, doi:10.1002/qj.134.

Kalesse, H., W. Szyrmer, S. Kneifel, P. Kollias, and E. Luke, 2016: Fingerprints of a riming event on cloud radar Doppler spectra: Observations and modeling. *Atmos. Chem. Phys.*, **16**, 2997–3012, doi:10.5194/acp-16-2997-2016.

Kanitz, T., P. Seifert, A. Ansmann, R. Engelmann, D. Althausen, C. Casiccia, and E. G. Rohwer, 2011: Contrasting the impact of aerosols at northern and southern midlatitudes on heterogeneous ice formation. *Geophys. Res. Lett.*, **38**, L17802, doi:10.1029/2011GL048532.

Kay, J. E., T. L'Ecuyer, A. Gettelman, G. L. Stephens, and C. O'Dell, 2008: The contribution of cloud and radiation anomalies to the 2007 Arctic sea ice extent minimum. *Geophys. Res. Lett.*, **35**, L08503, doi:10.1029/2008GL033451.

Klingebiel, M., and Coauthors, 2015: Arctic low-level boundary layer clouds: In situ measurements and simulations of mono- and bimodal supercooled droplet size distributions at the top layer of liquid phase clouds. *Atmos. Chem. Phys.*, **15**, 617–631, doi:10.5194/acp-15-617-2015.

Kneifel, S., U. Löhnert, A. Battaglia, S. Crewell, and D. Siebler, 2010: Snow scattering signals in ground-based passive microwave radiometer measurements. *J. Geophys. Res. Atmos.*, **115**, D16214, doi:10.1029/2010JD013856.

——, M. S. Kulie, and R. Bennartz, 2011: A triple-frequency approach to retrieve microphysical snowfall parameters. *J. Geophys. Res.*, **116**, D11203, doi:10.1029/2010JD015430.

——, S. Redl, E. Orlandi, U. Löhnert, M. P. Cadeddu, D. D. Turner, and M. Chen, 2014: Absorption properties of supercooled

liquid water between 31 and 225 GHz: Evaluation of absorption models using ground-based observations. *J. Appl. Meteor. Climatol.*, **53**, 1028–1045, doi:10.1175/JAMC-D-13-0214.1.

——, A. von Lerber, J. Tiira, D. Moisseev, P. Kollias, and J. Leinonen, 2015: Observed relations between snowfall microphysics and triple-frequency radar measurements. *J. Geophys. Res. Atmos.*, **120**, 6034–6055, doi:10.1002/2015JD023156.

——, P. Kollias, A. Battaglia, J. Leinonen, M. Maahn, H. Kalesse, and F. Tridon, 2016: First observations of triple-frequency radar Doppler spectra in snowfall: Interpretation and applications. *Geophys. Res. Lett.*, **43**, 2225–2233, doi:10.1002/2015GL067618.

Kollias, P., B. A. Albrecht, and F. D. Marks, 2001: Raindrop sorting induced by vertical drafts in convective clouds. *Geophys. Res. Lett.*, **28**, 2787–2790, doi:10.1029/2001GL013131.

——, E. E. Clothiaux, M. A. Miller, B. A. Albrecht, G. L. Stephens, and T. P. Ackerman, 2007: Millimeter-wavelength radars. *Bull. Amer. Meteor. Soc.*, **88**, 1608–1624, doi:10.1175/BAMS-88-10-1608.

——, N. Bharadwaj, K. Widener, I. Jo, and K. Johnson, 2014: Scanning ARM cloud radars. Part I: Operational sampling strategies. *J. Atmos. Oceanic Technol.*, **31**, 569–582, doi:10.1175/JTECH-D-13-00044.1.

Kulie, M. S., M. J. Hiley, R. Bennartz, S. Kneifel, and S. Tanelli, 2014: Triple-frequency radar reflectivity signatures of snow: Observations and comparisons with theoretical ice particle scattering models. *J. Appl. Meteor. Climatol.*, **53**, 1080–1098, doi:10.1175/JAMC-D-13-066.1.

Lack, S. A., and N. I. Fox, 2007: An examination of the effect of wind drift on radar-derived surface rainfall estimations. *Atmos. Res.*, **85**, 217–229, doi:10.1016/j.atmosres.2006.09.010.

Lauri, T., J. Koistinen, and D. Moisseev, 2012: Advection-based adjustment of radar measurements. *Mon. Wea. Rev.*, **140**, 1014–1022, doi:10.1175/MWR-D-11-00045.1.

Laviola, S., and V. Levizzani, 2011: The 183-WSL fast rain rate retrieval algorithm: Part I: Retrieval design. *Atmos. Res.*, **99**, 443–461, doi:10.1016/j.atmosres.2010.11.013.

Lohmann, U., F. Lüönd, and F. Mahrt, 2016: *Introduction to Clouds: From the Microscale to Climate.* Cambridge University Press, 399 pp., doi:10.1017/CBO9781139087513.

Löhnert, U., S. Kneifel, A. Battaglia, M. Hagen, L. Hirsch, and S. Crewell, 2011: A multisensor approach toward a better understanding of snowfall microphysics: The TOSCA project. *Bull. Amer. Meteor. Soc.*, **92**, 613–628, doi:10.1175/2010BAMS2909.1.

Luke, E. P., and P. Kollias, 2013: Separating cloud and drizzle radar moments during precipitation onset using Doppler spectra. *J. Atmos. Oceanic Technol.*, **30**, 1656–1671, doi:10.1175/JTECH-D-11-00195.1.

——, ——, and M. D. Shupe, 2010: Detection of supercooled liquid in mixed-phase clouds using radar Doppler spectra. *J. Geophys. Res.*, **115**, D19201, doi:10.1029/2009JD012884.

Maahn, M., and U. Löhnert, 2017: Potential of higher order moments of the radar Doppler spectrum for retrieving microphysical and kinematic properties of Arctic ice clouds. *J. Appl. Meteor. Climatol.*, **56**, 263–282, doi:10.1175/JAMC-D-16-0020.1.

——, C. Burgard, S. Crewell, I. V. Gorodetskaya, S. Kneifel, S. Lhermitte, K. Van Tricht, and N. P. M. van Lipzig, 2014: How does the spaceborne radar blind zone affect derived surface snowfall statistics in polar regions? *J. Geophys. Res. Atmos.*, **119**, 13 604–13 620, doi:10.1002/2014JD022079.

——, U. Löhnert, P. Kollias, R. C. Jackson, and G. M. McFarquhar, 2015: Developing and evaluating ice cloud parameterizations for forward modeling of radar moments using in situ aircraft observations. *J. Atmos. Oceanic Technol.*, **32**, 880–903, doi:10.1175/JTECH-D-14-00112.1.

Mace, G. G., and Q. Zhang, 2014: The CloudSat radar-lidar geometrical profile product (RL-GeoProf): Updates, improvements, and selected results. *J. Geophys. Res. Atmos.*, **119**, 9441–9462, doi:10.1002/2013JD021374.

Mamouri, R. E., and A. Ansmann, 2015: Estimated desert-dust ice nuclei profiles from polarization lidar: Methodology and case studies. *Atmos. Chem. Phys.*, **15**, 3463–3477, doi:10.5194/acp-15-3463-2015.

Marchand, R., G. G. Mace, T. Ackerman, and G. Stephens, 2008: Hydrometeor detection using *Cloudsat*—An Earth-orbiting 94-GHz cloud radar. *J. Atmos. Oceanic Technol.*, **25**, 519–533, doi:10.1175/2007JTECHA1006.1.

——, T. Ackerman, M. Smyth, and W. B. Rossow, 2010: A review of cloud top height and optical depth histograms from MISR, ISCCP, and MODIS. *J. Geophys. Res.*, **115**, D16206, doi:10.1029/2009JD013422.

Marshall, J. S., 1953: Precipitation trajectories and patterns. *J. Meteor.*, **10**, 25–29, doi:10.1175/1520-0469(1953)010<0025:PTAP>2.0.CO;2.

Mather, J. H., and J. W. Voyles, 2013: The ARM Climate Research Facility: A review of structure and capabilities. *Bull. Amer. Meteor. Soc.*, **94**, 377–392, doi:10.1175/BAMS-D-11-00218.1.

May, P. T., J. H. Mather, G. Vaughan, C. Jakob, G. M. McFarquhar, K. N. Bower, and G. G. Mace, 2008: The Tropical Warm Pool International Cloud Experiment. *Bull. Amer. Meteor. Soc.*, **89**, 629, doi:10.1175/BAMS-89-5-629.

Miller, M. A., K. Nitschke, T. P. Ackerman, W. R. Ferrell, N. Hickmon, and M. Ivey, 2016: The ARM Mobile Facilities. *The Atmospheric Radiation Measurement (ARM) Program: The First 20 Years*, *Meteor. Monogr.*, No. 57, Amer. Meteor. Soc., doi:10.1175/AMSMONOGRAPHS-D-15-0051.1.

Mishchenko, M. I., 2000: Calculation of the amplitude matrix for a nonspherical particle in a fixed orientation. *Appl. Opt.*, **39**, 1026–1031, doi:10.1364/AO.39.001026.

Mittermaier, P. M., J. R. Hogan, and J. A. Illingworth, 2004: Using mesoscale model winds for correcting wind-drift errors in radar estimates of surface rainfall. *Quart. J. Roy. Meteor. Soc.*, **130**, 2105–2123, doi:10.1256/qj.03.156.

Morrison, H., G. de Boer, G. Feingold, J. Harrington, M. D. Shupe, and K. Sulia, 2012: Resilience of persistent Arctic mixed-phase clouds. *Nat. Geosci.*, **5**, 11–17, doi:10.1038/ngeo1332.

Murtagh, D., and Coauthors, 2002: An overview of the Odin atmospheric mission. *Can. J. Phys.*, **80**, 309–319, doi:10.1139/p01-157.

Myagkov, A., P. Seifert, U. Wandinger, M. Bauer-Pfundstein, and S. Y. Matrosov, 2015: Effects of antenna patterns on cloud radar polarimetric measurements. *J. Atmos. Oceanic Technol.*, **32**, 1813–1828, doi:10.1175/JTECH-D-15-0045.1.

——, ——, M. Bauer-Pfundstein, and U. Wandinger, 2016: Cloud radar with hybrid mode towards estimation of shape and orientation of ice crystals. *Atmos. Meas. Tech.*, **9**, 469–489, doi:10.5194/amt-9-469-2016.

Naud, C., J. F. Booth, and A. D. Del Genio, 2014: Evaluation of ERA-Interim and MERRA cloudiness in the Southern Ocean. *J. Climate*, **27**, 2109–2124, doi:10.1175/JCLI-D-13-00432.1.

Pal, S. R., W. Steinbrecht, and A. I. Carswell, 1992: Automated method for lidar determination of cloud-base height and vertical extent. *Appl. Opt.*, **31**, 1488–1494, doi:10.1364/AO.31.001488.

Petty, G. W., 2006: *A First Course in Atmospheric Radiation.* 2nd ed. Sundog, 459 pp.

Pilewskie, P., and S. Twomey, 1987: Discrimination of ice from water in clouds by optical remote sensing. *Atmos. Res.*, **21**, 113–122, doi:10.1016/0169-8095(87)90002-0.

——, and Coauthors, 2003: Solar spectral radiative forcing during the Southern African Regional Science Initiative. *J. Geophys. Res.*, **108**, 8486, doi:10.1029/2002JD002411.

Protat, A., and Coauthors, 2009: Assessment of Cloudsat reflectivity measurements and ice cloud properties using ground-based and airborne cloud radar observations. *J. Atmos. Oceanic Technol.*, **26**, 1717–1741, doi:10.1175/2009JTECHA1246.1.

——, J. Delanoë, E. J. O'Connor, and T. S. L'Ecuyer, 2010: The evaluation of Cloudsat and CALIPSO ice microphysical products using ground-based cloud radar and lidar observations. *J. Atmos. Oceanic Technol.*, **27**, 793–810, doi:10.1175/2009JTECHA1397.1.

Pruppacher, H. R., and J. D. Klett, 1997: *Microphysics of Clouds and Precipitation.* 2nd ed. Kluwer Academic, 954 pp.

Rambukkange, M. P., J. Verlinde, E. W. Eloranta, C. J. Flynn, and E. E. Clothiaux, 2011: Using Doppler spectra to separate hydrometeor populations and analyze ice precipitation in multilayered mixed-phase clouds. *IEEE Geosci. Remote Sens. Lett.*, **8**, 108–112, doi:10.1109/LGRS.2010.2052781.

Rosenfeld, D., and Coauthors, 2014: Global observations of aerosol-cloud-precipitation-climate interactions. *Rev. Geophys.*, **52**, 750–808, doi:10.1002/2013RG000441.

Sassen, K., and J. Zhu, 2009: A global survey of CALIPSO linear depolarization ratios in ice clouds: Initial findings. *J. Geophys. Res.*, **114**, D00H07, doi:10.1029/2009JD012279.

——, Z. Wang, and D. Liu, 2008: Global distribution of cirrus clouds from CloudSat/Cloud-Aerosol Lidar and Infrared Pathfinder Satellite Observations (CALIPSO) measurements. *J. Geophys. Res.*, **113**, D00A12, doi:10.1029/2008JD009972.

——, ——, and ——, 2009: Cirrus clouds and deep convection in the tropics: Insights from CALIPSO and CloudSat. *J. Geophys. Res.*, **114**, D00H06, doi:10.1029/2009JD011916.

Sato, K., and H. Okamoto, 2006: Characterization of Z and LDR of nonspherical and inhomogeneous ice particles for 95-GHz cloud radar: Its implication to microphysical retrievals. *J. Geophys. Res.*, **111**, D22213, doi:10.1029/2005JD006959.

Schäfer, M., E. Bierwirth, A. Ehrlich, E. Jäkel, and M. Wendisch, 2015: Airborne observations and simulations of three-dimensional radiative interactions between Arctic boundary layer clouds and ice floes. *Atmos. Chem. Phys.*, **15**, 8147–8163, doi:10.5194/acp-15-8147-2015.

Schmidt, K. S., and Coauthors, 2010: A new method for deriving aerosol solar radiative forcing and its first application within MILAGRO/INTEX-B. *Atmos. Chem. Phys.*, **10**, 7829–7843, doi:10.5194/acp-10-7829-2010.

Scott, E. G., D. M. Babb, and J. Verlinde, 2001: Processing millimeter wave profiler radar spectra. *J. Atmos. Oceanic Technol.*, **18**, 1577–1583, doi:10.1175/1520-0426(2001)018<1577:PMWPRS>2.0.CO;2.

Seifert, P., and Coauthors, 2010: Saharan dust and heterogeneous ice formation: Eleven years of cloud observations at a central European EARLINET site. *J. Geophys. Res.*, **115**, D20201, doi:10.1029/2009JD013222.

——, and Coauthors, 2015: Seasonal variability of heterogeneous ice formation in stratiform clouds over the Amazon Basin. *Geophys. Res. Lett.*, **42**, 5587–5593, doi:10.1002/2015GL064068.

Shupe, M. D., P. Kollias, S. Y. Matrosov, and T. L. Schneider, 2004: Deriving mixed-phase cloud properties from Doppler radar spectra. *J. Atmos. Oceanic Technol.*, **21**, 660–670, doi:10.1175/1520-0426(2004)021<0660:DMCPFD>2.0.CO;2.

——, ——, P. O. G. Persson, and G. M. McFarquhar, 2008: Vertical motions in Arctic mixed-phase stratiform clouds. *J. Atmos. Sci.*, **65**, 1304–1322, doi:10.1175/2007JAS2479.1.

——, and Coauthors, 2013: High and dry: New observations of tropospheric and cloud properties above the Greenland Ice Sheet. *Bull. Amer. Meteor. Soc.*, **94**, 169–186, doi:10.1175/BAMS-D-11-00249.1.

Skofronick-Jackson, G., and Coauthors, 2015: Global Precipitation Measurement Cold Season Precipitation Experiment (GCPEX): For measurement's sake, let it snow. *Bull. Amer. Meteor. Soc.*, **96**, 1719–1741, doi:10.1175/BAMS-D-13-00262.1.

Smith, E. A., and Coauthors, 2007: International Global Precipitation Measurement (GPM) Program and Mission: An overview. *Measuring Precipitation from Space*, V. Levizzani, P. Bauer, and F. J. Turk, Eds., Advances in Global Change Research Series, Vol. 28, Springer, 611–653.

Stein, T. H. M., D. J. Parker, J. Delanoë, N. S. Dixon, R. J. Hogan, P. Knippertz, R. I. Maidment, and J. H. Marsham, 2011: The vertical cloud structure of the West African monsoon: A 4 year climatology using CloudSat and CALIPSO. *J. Geophys. Res.*, **116**, D22205, doi:10.1029/2011JD016029.

Stephens,G. L., and Coauthors, 2002: The CloudSat mission and the A-Train: A new dimension of space-based observations of clouds and precipitation. *Bull. Amer. Meteor. Soc.*, **83**, 1771–1790, doi:10.1175/BAMS-83-12-1771.

Sun, N., and F. Weng, 2012: Retrieval of cloud ice water path from Special Sensor Microwave Imager/Sounder (SSMIS). *J. Appl. Meteor. Climatol.*, **51**, 366–379, doi:10.1175/JAMC-D-11-021.1.

Surussavadee, C., and D. H. Staelin, 2009: Satellite retrievals of Arctic and equatorial rain and snowfall rates using millimeter wavelengths. *IEEE Trans. Geosci. Remote Sens.*, **47**, 3697–3707, doi:10.1109/TGRS.2009.2029093.

Thompson, E. J., S. A. Rutledge, B. Dolan, V. Chandrasekar, and B. L. Cheong, 2014: A dual-polarization radar hydrometeor classification algorithm for winter precipitation. *J. Atmos. Oceanic Technol.*, **31**, 1457–1481, doi:10.1175/JTECH-D-13-00119.1.

Thorsen, T. J., Q. Fu, and J. Comstock, 2011: Comparison of the CALIPSO satellite and ground-based observations of cirrus clouds at the ARM TWP sites. *J. Geophys. Res.*, **116**, D21203, doi:10.1029/2011JD015970.

Trenberth, K. E., and J. T. Fasullo, 2010: Simulation of present-day and twenty-first-century energy budgets of the southern oceans. *J. Climate*, **23**, 440–454, doi:10.1175/2009JCLI3152.1.

Van Tricht, K., I. V. Gorodetskaya, S. Lhermitte, D. D. Turner, J. H. Schween, and N. P. M. Van Lipzig, 2014: An improved algorithm for polar cloud-base detection by ceilometer over the ice sheets. *Atmos. Meas. Tech.*, **7**, 1153–1167, doi:10.5194/amt-7-1153-2014.

Vaughan, M. A., and Coauthors, 2009: Fully automated detection of cloud and aerosol layers in the CALIPSO lidar measurements. *J. Atmos. Oceanic Technol.*, **26**, 2034–2050, doi:10.1175/2009JTECHA1228.1.

Verlinde, J., M. P. Rambukkange, E. E. Clothiaux, G. M. McFarquhar, and E. W. Eloranta, 2013: Arctic multilayered, mixed-phase cloud processes revealed in millimeter-wave cloud radar Doppler spectra. *J. Geophys. Res. Atmos.*, **118**, 13 199–13 213, doi:10.1002/2013JD020183.

Verlinden, K. L., D. W. J. Thompson, and G. L. Stephens, 2011: The three-dimensional distribution of clouds over the

Southern Hemisphere high latitudes. *J. Climate*, **24**, 5799–5811, doi:10.1175/2011JCLI3922.1.

Voigt, C., and Coauthors, 2017: ML-CIRRUS: The airborne experiment on natural cirrus and contrail cirrus with the high-altitude long-range research aircraft HALO. *Bull. Amer. Meteor. Soc.*, **98**, 271–288, doi:10.1175/BAMS-D-15-00213.1.

Wang, J. R., P. E. Racette, J. R. E. Piepmeier, B. Monosmith, and W. Manning, 2007: Airborne CoSMIR observations between 50 and 183 GHz over snow-covered Sierra Mountains. *IEEE Trans. Geosci. Remote Sens.*, **45**, 55–61, doi:10.1109/TGRS.2006.885410.

Wang, Z., and Coauthors, 2012: Single aircraft integration of remote sensing and in situ sampling for the study of cloud microphysics and dynamics. *Bull. Amer. Meteor. Soc.*, **93**, 653–668, doi:10.1175/BAMS-D-11-00044.1.

Waters, J. W., and Coauthors, 2006: The Earth Observing System Microwave Limb Sounder (EOS MLS) on the Aura satellite. *IEEE Trans. Geosci. Remote Sens.*, **44**, 1075–1092, doi:10.1109/TGRS.2006.873771.

Wendisch, M., and A. Ehrlich, 2011: Bodengebunde und flugzeuggetragene passive Fernerkundung von Wolken mit Hilfe von solaren Strahlungsmessungen (Ground and airborne passive remote sensing of clouds by means of solar radiation measurements). *Promet*, **36**, 119–128.

——, and J. L. Brenguier, Eds., 2013: *Airborne Measurements for Environmental Research: Methods and Instruments*. John Wiley & Sons, 641 pp.

——, J. Heintzenberg, and M. Bussemer, 2001: Measurement-based aerosol forcing calculations: The influence of model complexity. *Meteor. Z.*, **10**, 45–60, doi:10.1127/0941-2948/2001/0010-0045.

——, P. Yang, and A. Ehrlich, 2013a: Amplified climate changes in the Arctic: Role of clouds and atmospheric radiation. *Conference Reports of the Mathematical and Natural Sciences*, Vol. 132, Saxon Academy of Sciences, 34 pp.

——, and Coauthors, 2013b: Atmospheric radiation measurements. *Airborne Measurements for Environmental Research: Methods and Instruments*, M. Wendisch and J.-L. Brenguier, Eds., Wiley, 343–411.

——, and Coauthors, 2016: The ACRIDICON–CHUVA campaign: Studying tropical deep convective clouds and precipitation over Amazonia using the new German research aircraft HALO. *Bull. Amer. Meteor. Soc.*, **97**, 1885–1908, 10.1175/BAMS-D-14-00255.1.

——, and Coauthors, 2017: Understanding causes and effects of rapid warming in the Arctic. *Eos, Trans. Amer. Geophys. Union*, **98**, doi:10.1029/2017EO064803.

Werner, F., H. Siebert, P. Pilewskie, T. Schmeissner, R. A. Shaw, and M. Wendisch, 2013: New airborne retrieval approach for trade wind cumulus properties under overlying cirrus. *J. Geophys. Res. Atmos.*, **118**, 3634–3649, doi:10.1002/jgrd.50334.

——, and Coauthors, 2014: Twomey effect observed from collocated microphysical and remote sensing measurements over shallow cumulus. *J. Geophys. Res. Atmos.*, **119**, 1534–1545, doi:10.1002/2013JD020131.

Westbrook, C. D., and A. J. Illingworth, 2013: The formation of ice in a long-lived supercooled layer cloud. *Quart. J. Roy. Meteor. Soc.*, **139**, 2209–2221, doi:10.1002/qj.2096.

Winker, D. M., M. A. Vaughan, A. Omar, Y. Hu, K. A. Powell, Z. Liu, W. H. Hunt, and S. A. Young, 2009: Overview of the CALIPSO mission and CALIOP data processing algorithms. *J. Atmos. Oceanic Technol.*, **26**, 2310–2323, doi:10.1175/2009JTECHA1281.1.

——, and Coauthors, 2010: The CALIPSO mission: A global 3D view of aerosols and clouds. *Bull. Amer. Meteor. Soc.*, **91**, 1211–1229, doi:10.1175/2010BAMS3009.1.

Wu, D. L., and Coauthors, 2008: Validation of the Aura MLS cloud ice water content measurements. *J. Geophys. Res.*, **113**, D15S10, doi:10.1029/2007JD008931.

——, and Coauthors, 2009: Comparisons of global cloud ice from MLS, CloudSat, and correlative data sets. *J. Geophys. Res.*, **114**, D00A24, doi:10.1029/2008JD009946.

Xie, X., U. Löhnert, S. Kneifel, and S. Crewell, 2012: Snow particle orientation observed by ground-based microwave radiometry. *J. Geophys. Res.*, **117**, D02206, doi:10.1029/2011JD016369.

——, S. Crewell, U. Löhnert, C. Simmer, and J. Miao, 2015: Polarization signatures and brightness temperatures caused by horizontally oriented snow particles at microwave bands: Effects of atmospheric absorption. *J. Geophys. Res. Atmos.*, **120**, 6145–6160, doi:10.1002/2015JD023158.

Yoshida, R., H. Okamoto, Y. Hagihara, and H. Ishimoto, 2010: Global analysis of cloud phase and ice crystal orientation from Cloud-Aerosol Lidar and Infrared Pathfinder Satellite Observation (CALIPSO) data using attenuated backscattering and depolarization ratio. *J. Geophys. Res.*, **115**, D00H32, doi:10.1029/2009JD012334.

Zawadzki, I., F. Fabry, and W. Szyrmer, 2001: Observations of supercooled water and secondary ice generation by a vertically pointing X-band Doppler radar. *Atmos. Res.*, **59**, 343–359, doi:10.1016/S0169-8095(01)00124-7.

Zhang, K., X. Liu, M. Wang, J. M. Comstock, D. L. Mitchell, S. Mishra, and G. G. Mace, 2013: Evaluating and constraining ice cloud parameterizations in CAM5 using aircraft measurements from the SPARTICUS campaign. *Atmos. Chem. Phys.*, **13**, 4963–4982, doi:10.5194/acp-13-4963-2013.

Zhang, Y., S. A. Klein, J. Boyle, and G. G. Mace, 2010: Evaluation of tropical cloud and precipitation statistics of Community Atmosphere Model version 3 using CloudSat and CALIPSO data. *J. Geophys. Res.*, **115**, D12205, doi:10.1029/2009JD012006.